Z LINESHAPE MEASUREMENT WITH THE ALEPH DETECTOR

by

ZHONG FENG

A dissertation submitted in partial fulfillment

of the requirements for the degree of

Doctor of Philosophy

(Physics)

at the

UNIVERSITY OF WISCONSIN-MADISON

1995

Z LINESHAPE MEASUREMENT WITH THE ALEPH DETECTOR

Zhong Feng

Under the supervision of Professor Sau Lan Wu

At the University of Wisconsin–Madison

ABSTRACT

A measurement of Z lineshape parameters has been made with the ALEPH detector in a high precision three-point energy scan across the Z resonance at the LEP e^+e^- collider in 1993. By using the spin resonance depolarization method, the LEP beam energy at each scan point was measured with high precision. With the help of increased luminosity at each energy scan point, we have a better understanding of background and systematic uncertainties. Based on all data taken since 1989, the resonance parameters of Z are determined to be $M_Z = (91.1916 \pm 0.0039)$ GeV, $\Gamma_Z = (2.4941 \pm 0.0058)$ GeV, $\sigma^0_{had} = (41.63 \pm 0.10)$ nb, and $R_l = 20.751 \pm 0.074$. The corresponding number of light neutrino species is $N_\nu = 2.966 \pm 0.024$. Combining this with ALEPH measurements of the lepton forward-backward asymmetry, b and c quark asymmetries, and τ polarization, a constraint on the top quark mass of $M_{top} = 178^{+15}_{-16}\ ^{+16}_{-18}$ GeV is obtained in the context of the Standard Model.

Acknowledgements

First of all, I would like to thank my advisor, Sau Lan Wu, who provided me the great opportunity to work for the ALEPH experiment with her unique Wisconsin group at CERN. She has successfully established a group composed of many brilliant young physicists and a powerful computer environment and resources from which I have greatly benefited in my dissertation. Her dedication and enthusiasm to the professional field has generated a strong influence over me and many young physicists in the group. Her constant encouragement and guidance have been a driving force behind this work.

I am also deeply indebted to many young physicists in the group for their invaluable help in this dissertation and in my detector hardware training. Robert Johnson showed me the intricate procedures of the TPC dE/dx calibration, and helped me to become an expert in this area. John Conway led me into the field of the TPC electronics calibration. His great responsibility to the work and persistent effort in doing the best job have greatly influenced me. John Harton introduced me to the hadronic event selection analysis and the Z lineshape fit. His inspiration and advice have been an indispensable part of the whole process of this analysis.

Outside the group, I am very grateful to the opportunity working with Werner Witzeling, Ron Settles, and Pere Mato on the daily operation and maintenance of the TPC. Their capability in problem solving has greatly impressed me. I would like to thank Alain Blondel, who helped me to understand the complex nature of the LEP energy calibration and the mystery of electroweak radiative corrections. His suggestions on the point to point hadronic event selection efficiency study and two photon background estimation have made an important part of this analysis.

There are many graduate students and young physicists with whom I have been working and sharing the wisdom and pleasure. To name a few: Leo Bellantoni and Doug Ferguson on the TPC electronics calibration; Michael Schmitt and Jane Nachtman on the TPC dE/dx calibration; Jim Grahl and Arnaud Lucotte on the TPC hadronic event selection; Manel Martinez, Wei Chen and Frederic Teubert on the Z lineshape fit.

John Harton, Alain Blondel, John Yamartino, Michael Walsh, and Jim Grahl have taken a lot of time to offer comments and criticism of my thesis. Their valuable comments and corrections substantially improve the quality of this work. Huizheng Gao deserves my special thanks for the help of making good diagrams.

I would like to express my thanks to Haimo Zobernig, Chris Lishka, and Sloan Looney for their high quality service work and friendly technical help on the computers. I also want to thank our group secretaries Patricia Van Gene and Shelly McKenzie for the help during my stay at CERN.

Finally I would like to thank my wife, Min Zheng for her love and under-

standing during those seemingly endless graduate student years, and I would like to thank my parents for their constant support and encouragement. I also want to thank my former advisor Minghan Ye for introducing me to this exciting field of high energy physics.

Contents

Chapter 1

Introduction

It is believed that there are four basic forces, namely gravitation, electromagnetism, the weak force and the strong nuclear force. The interactions of the last three forces with matter can be explained as being mediated by so called gauge particles. The Standard Model [1], developed in the early 70's, unifies the electromagnetic and weak forces into a combined electroweak interaction and models the strong interaction using quantum chromodynamics [2]. The photon, γ, and the weak vector bosons, W^+, W^- and Z, are the mediating gauge particles for the unified electroweak interaction.

In the past twenty five years, the Standard Model has been extensively tested and verified by experiments [3]. No experimental evidence has been found to disprove the model. The construction of the e^+e^- colliders LEP and SLC [4], has offered the opportunity to extend these tests of the theory to the Z mass region with very high precision.

As a vector boson, the Z may decay into any kinematically available

fermions and anti-fermion pair. By measuring the cross sections $\sigma(e^+e^- \rightarrow Z \rightarrow f\bar{f})$ as a function of center-of-mass energy $\sqrt{s}$ around the Z mass M_Z, a Breit-Wigner resonance lineshape is observed. By fitting the Z resonance lineshape we can extract the basic parameters such as the mass M_Z, the width Γ_Z, and the peak cross section, σ^0_{ff}. The precise measurement of these parameters is of great interest. As we will see, M_Z can be measured with an extremely good precision, about 2×10^{-5}. This precision on M_Z (the last missing input parameter) precisely fixes the Standard Model predictions at tree level. On the other hand, Γ_Z and σ^0_{ff} can be used to precisely test the model predictions. By assuming that Standard Model is correct, the Γ_Z measurements can also be used to constrain the top quark mass, which is directly measured in the CDF and D0 experiment [5][6].

In this dissertation, measurements of the hadronic cross section are made using data collected with ALEPH detector during LEP's 1993 three-point energy scan across the Z resonance. A Z lineshape fit is performed using a model independent formula from which the electroweak parameters M_Z, Γ_Z and peak hadronic cross section σ^0_{had} are extracted. Combining with other electroweak parameters measured by ALEPH, a constraint for the top quark mass is obtained in the context of the Standard Model.

Chapter 2 describes the LEP machine and the ALEPH detector. Chapter 3 is dedicated to the hadronic cross section measurements of 1993 data. Chapter 4 shows the Z lineshape fitting procedures and the results. The remainder of this chapter is devoted to a brief overview of the electroweak theory of the Standard Model at the Z resonance and a description of a model

independent lineshape fit formula, with which the electroweak parameters are extracted.

1.1 Standard Model and Z resonance

The Standard Model (SM) requires the presence of three massive vector bosons, the Z, W^+ and W^- to mediate weak interactions [7]. In order to introduce masses for the fermions and bosons, a further scalar boson, the Higgs (H^0), has to be postulated [8].

In the SM, the fermions are grouped into families according to weak isospin; doublets for left-handed fermions and singlets for right-handed fermions [9]. The known lepton families are:

$$\begin{pmatrix} \nu_e \\ e \end{pmatrix}_L \begin{pmatrix} \nu_\mu \\ \mu \end{pmatrix}_L \begin{pmatrix} \nu_\tau \\ \tau \end{pmatrix}_L \quad e_R, \mu_R, \tau_R$$

The known quark families are:

$$\begin{pmatrix} u \\ d \end{pmatrix}_L \begin{pmatrix} c \\ s \end{pmatrix}_L \begin{pmatrix} t \\ b \end{pmatrix}_L \quad \begin{pmatrix} u \\ d \end{pmatrix}_R \begin{pmatrix} c \\ s \end{pmatrix}_R \begin{pmatrix} t \\ b \end{pmatrix}_R$$

So far the neutrinos appear to be essentially massless, and experimental results showed [10] that only left-handed neutrinos exist. Quarks are the basic constituent of hadrons and participate in all kind of interactions, while the leptons only participate in electroweak interactions.

At the lowest order approximation (so called tree level) in the SM, the $e^+e^- \to f\bar{f}$ processes can be described with three parameters. These three free parameters are usually expressed in terms of quantities known to the best accuracy. At the Z resonance, a common choice is: electromagnetic coupling constant, α_{em}, the Fermi coupling constant, G_F, and M_Z. Table 1.1 lists updated values of these three parameters [4] [11].

Parameter	Measured Value	Precision
α_{em}	$[137.0359895(61)]^{-1}$	4.5×10^{-8}
G_F	$1.166372(2) \times 10^{-5} GeV^{-2}$	1.7×10^{-5}
M_Z	$91.1887(22) GeV$	2.4×10^{-5}

Table 1.1: Measured values of three basic Standard Model parameters.

Due to the Z resonance, the $e^+e^- \to (\gamma, Z) \to f\bar{f}$ cross section (shown in Figure 1.1.) is greatly enhanced [12] around Z mass energy region. At tree level, the cross section of $e^+e^- \to (\gamma, Z) \to f\bar{f}$ (with $f \neq e$) can be calculated via the diagrams shown in Figure 1.2 as [13]:

$$\sigma_{ff}(s) = \frac{s}{(s-M_Z^2)^2 + s^2\Gamma_Z^2/M_Z^2}\left(\sigma_{ff}^0\Gamma_Z^2 + I_f\frac{N_c^f(s-M_Z^2)}{s}\right) + \frac{4}{3}\pi N_c^f Q_f^2\frac{\alpha_{em}^2}{s}\ , \tag{1.1}$$

where σ_{ff}^0 is the peak cross section at $\sqrt{s} = M_Z$. Q_f is the electrical charge and N_c is the colour factor[1] of the fermion. In the formula, the first term is

[1]According to Quantum Chromodynamics (QCD), a quark has three colors, namely red, green and blue. The leptons are colorless and N_c =1.

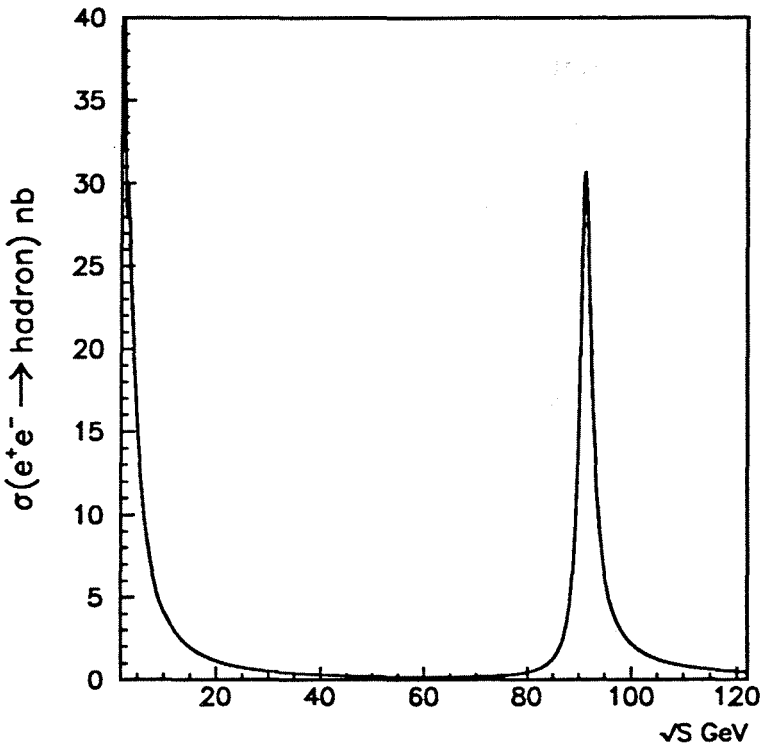

Figure 1.1: Hadronic cross section as function of center-of-mass energy

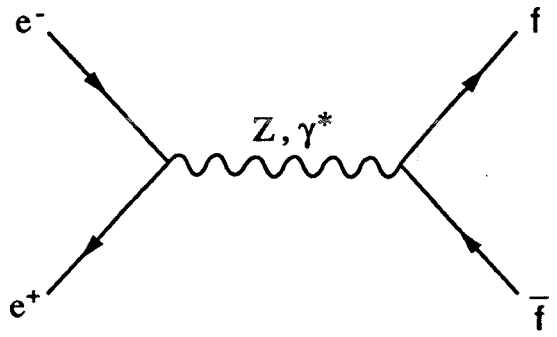

Figure 1.2: Feynman diagrams for the process $e^+e^- \to \gamma, Z \to f\bar{f}$.

from the Z exchange process, which is greatly enhanced by the Breit-Wigner form factor at the center-of-mass energies near the Z mass; the second term, multiplied by I_f is from the $Z-\gamma$ interference process; the third term is from the photon exchange process. In the Z resonance region, the contributions from the $Z-\gamma$ interference account for a small ($\mathcal{O}(1\%)$) part of the total cross section. For the Z hadronic decays, the photon exchange process contributes about 1% to the cross sections across the Z resonance.

The peak cross section σ^0_{ff} can be expressed as:

$$\sigma^0_{ff} = \frac{12\pi\Gamma_e\Gamma_{ff}}{M_Z^2\Gamma_Z^2}$$

where Γ_e and Γ_{ff} are the partial widths for Z decay into an e^+e^- and any fermion pair $f\bar{f}$ respectively. In the SM at the lowest order, the partial widths can be written as:

$$\Gamma_{ff} = \frac{G_F M_Z^3}{6\pi\sqrt{2}}((g_V^f)^2 + (g_A^f)^2)\cdot N_c \ ,$$

where g_V^f and g_A^f are the vector and axial-vector coupling constants of the Z to fermion f, They can be expressed as:

$$\begin{aligned} g_V^f &= I_3^f - 2Q_f sin^2\theta_W \\ g_A^f &= I_3^f \ . \end{aligned}$$

Here I_3^f is the third component of the weak isospin of the fermion. θ_W is the

weak angle of the SM and $sin^2\theta_W = 1 - M_W^2/M_Z^2$ in the tree level. Table 1.1 shows some numerical values of quantum numbers, the coupling constants for the four types of fermions.

f	I_3^f	Q_f	g_A^f	g_V^f
ν	1/2	0	1/2	1/2
e	-1/2	-1	-1/2	-0.04
u	1/2	2/3	1/2	0.19
d	-1/2	-1/3	-1/2	-0.35

Table 1.2: Quantum numbers and coupling constants of four types of fermions. Here $sin^2\theta_W = 0.23$ is taken.

1.2 Radiative corrections

To match the precision of the data at LEP, higher order corrections (so-called "radiative corrections") have to be included in the theoretical cross section and partial width calculations.

At the initial state, the largest correction comes from initial state radiation (ISR), where a photon is radiated from initial state particles (e^+ *or* e^-), thus modifying the effective center-of-mass energy. The ISR has a substantial effect on cross sections close to the Z resonance. As shown in Figure 1.3, after correcting for ISR, the peak hadronic cross section is decreased by about 30%.

For the final state, a QED radiative correction (photon emissions) has to

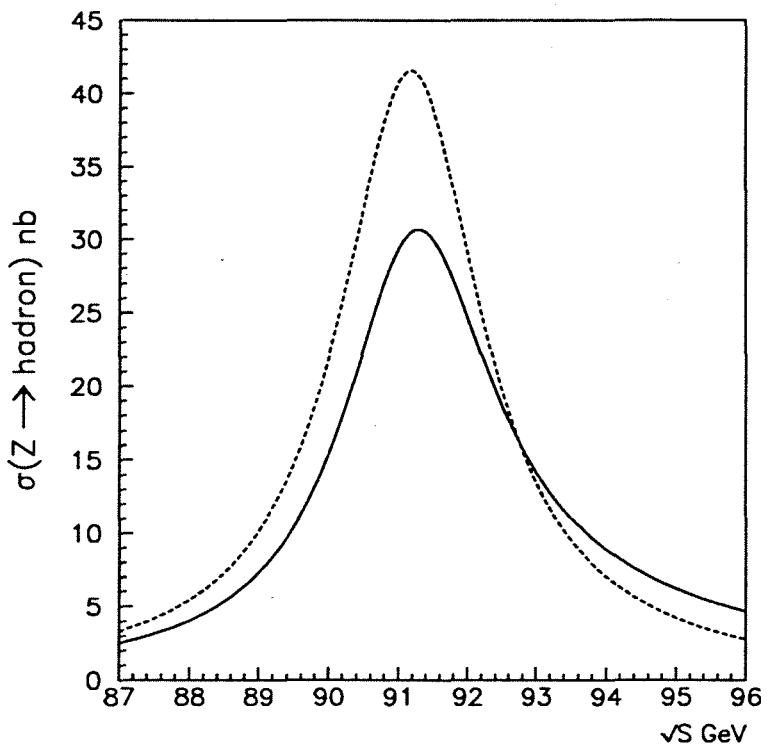

Figure 1.3: The effect of ISR on $\sigma(e^+e^- \to (\gamma, Z) \to q\bar{q})$. The dashed line is the SM calculation of hadronic cross sections assuming $M_Z = 91.1887$ GeV, without ISR. The solid line represents the hadronic cross sections with ISR.

be considered. With this correction, the Z partial width becomes [13]:

$$\Gamma_{ff} \to \Gamma_{ff}(1 + \Delta^f_{QED}) \ ,$$

$$\Delta^f_{QED} = \frac{3\alpha_{em}}{4\pi} Q_f \ .$$

For lepton partial widths, the correction is about 0.17%. For the hadronic final state, an additional radiative correction (gluon emission) has to be taken into account. This QCD correction has the following form [14]:

$$\Gamma_{q\bar{q}} \to \Gamma_{q\bar{q}}(1 + \Delta_{QCD}),$$

$$\Delta_{QCD} = \frac{\alpha_s(M_Z^2)}{\pi} + 1.409\left(\frac{\alpha_s(M_Z^2)}{\pi}\right)^2 - 12.805\left(\frac{\alpha_s(M_Z^2)}{\pi}\right)^3 + \ldots \ .$$

Here $\alpha_s(M_Z^2)$ is the strong interaction coupling constant at the Z mass. If we take the value measured from event shape at LEP, $\alpha_s(M_Z^2) = 0.123 \pm 0.006$ [15], this correction is estimated to be about $(4.05 \pm 0.19)\%$.

Taking into account all above corrections, we still have one set of more important corrections to be considered. These are the electroweak radiative corrections. They include the corrections on the vertex, and self-energy loops in the propagator line (see Figure 1.4). The interesting part of these corrections is that in the diagrams, the loop can be any particle pairs which couple to the Z or photon, even if they are much heavier than the available center-of-mass energy (for example, the top quark). This provides us a probe into the physics beyond the energy scale $\sqrt{s} = M_Z$. As we will show later, this is

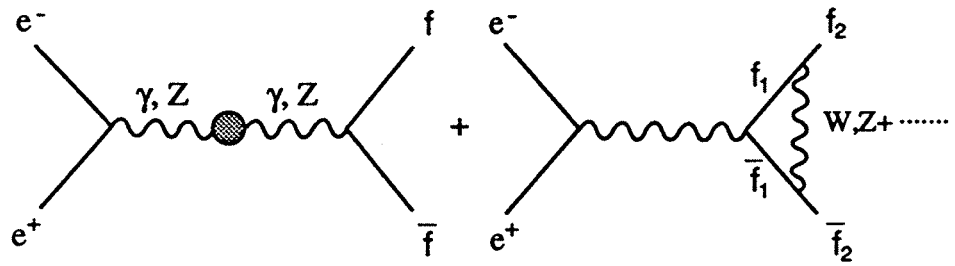

Figure 1.4: Feynman diagrams for the electroweak radiative corrections.

how the mass of the top quark was constrained before its direct observation in CDF at Fermilab [16]. The contribution from vertex corrections in the diagrams only become significant when Z decays into a pair of b quarks.

With the electroweak corrections, the electromagnetic coupling constant α_{em} becomes:

$$\alpha_{em} \rightarrow \alpha_{em}(s) = \frac{\alpha_{em}}{1 - \Delta\alpha_{em}(s)},$$

where $\Delta\alpha_{em}(M_Z^2) \approx 0.07$. Recently, there have been several reevaluations of $\alpha_{em}(M_Z^2)$ [17][18][19]. In this dissertation, a value of $\alpha_{em}(M_Z^2) = 1/128.896 \pm 0.090$ [19] is taken for consistency with the LEP electroweak working group.

After these corrections, the Z partial width, Γ_{ff}, becomes [3]:

$$\Gamma_{ff} = \frac{G_F M_Z^3}{6\pi\sqrt{2}}((\hat{g}_V^f)^2 + (\hat{g}_A^f)^2)\left(1 + \frac{3\alpha_{em}}{4\pi}\right) \cdot N_c^f \ (1 + \Delta_{QCD}^f) \ .$$

Here $\hat{g}_V^f$ and $\hat{g}_A^f$ are the effective coupling constants defined by:

$$\begin{aligned} \hat{g}_V^f &= \sqrt{\rho_f}(I_3^f - 2Q_f\kappa_f sin^2\theta_W) \\ \hat{g}_A^f &= \sqrt{\rho_f} I_3^f \ , \end{aligned}$$

where ρ_f and κ_f are the weak form factors. They contain the electroweak corrections including the dependence on M_{top} and M_H. In the on-shell scheme, $\rho_f = 1 + \Delta\rho \approx 1 + 3G_F M_{top}^2/8\sqrt{2}\pi^2$, and $\kappa_f \approx 1 - \Delta\rho/(1 - tan^2\theta_W)$. For $M_{top} = 176$ GeV, $\Delta\rho \simeq 0.01$. At LEP, an effective electroweak mixing angle is defined by:

$$sin^2\theta_W^{eff} \equiv \frac{1}{4}\left(1 - \frac{\hat{g}_V^l}{\hat{g}_A^l}\right) \quad ,$$

where $\hat{g}_V^l$ and $\hat{g}_A^l$ are the effective couplings for leptons.

For the partial width of Z decays into hadrons, in addition to the loop corrections, the vertex corrections have to be considered, especially for b quark final states [3]:

$$\Gamma_b = \Gamma_d(1 + \delta_{vb}),$$

where $\delta_{vb} \sim (-0.5M_{top}^2/M_Z^2 + 0.2)10^{-2} \simeq -1.66 \cdot 10^{-2}$. The hadronic partial width thus becomes:

$$\Gamma_{had} \equiv \Gamma_u + \Gamma_d + \Gamma_s + \Gamma_c + \Gamma_b \simeq 2\Gamma_u + (3 + \delta_{vb})\Gamma_d$$

The complete description of electroweak corrections are beyond scope of this dissertation and may be found in reference [20].

1.3 The Model independent description

From the cross sections measured across the Z resonance, the parameters M_Z, Γ_Z, and peak cross sections can be extracted. In order to compare

the fit results with various theoretical model predictions, ideally the fitting formula used to extract the results should be free of assumptions made by the theoretical models. The model independent description is a good approach to avoid possible bias made by the assumptions with theoretical models (such as the SM parameters top quark mass and Higgs mass for the partial width calculations), and allows easier interpretation of the model independent fit results in terms of new theoretical models.

MIZA (Model Independent Z Approximation), a model independent fitting software package has been developed to fit for the Z lineshape parameters at ALEPH [21]. It is based on the ideas that the Z resonance is well described in a Breit-Wigner form, and it assumes the validity of QED corrections for the $e^+e^- \to \gamma \to f\bar{f}$ processes, and uses QCD corrections which are empirically derived from lower energy data. The total cross section for the process $e^+e^- \to f\bar{f}$, thus can be expressed as:

$$\begin{aligned}
\sigma_{ff}(s) &= \frac{s}{(s-M_Z^2)^2 + s^2\Gamma_Z^2/M_Z^2} \cdot \frac{\sigma_{ff}^0 \Gamma_Z^2}{(1+\Delta_{QED}^e)} \\
&+ \frac{s}{(s-M_Z^2)^2 + s^2\Gamma_Z^2/M_Z^2} \cdot \left(I_f \frac{N_c^f (s-M_Z^2)}{s} (1+\Delta_{QCD}^f) \right) \\
&+ \frac{4}{3}\pi \cdot Q_f^2 \cdot \frac{\alpha_{em}^2(s)}{s} \cdot N_c^f (1+\Delta_{QCD}^f) \ . \qquad (1.2)
\end{aligned}$$

Here the Z mass, total width and partial widths, the peak cross sections are treated as free and independent physical parameters.

The ISR correction, is included by convoluting a radiator function $H(s,s')$

with the cross section $\sigma_{ff}(s)$:

$$\sigma'_{ff}(s) = \int_{s'=s_{min}}^{s'=s} H(s,s')\sigma_{ff}(s')ds' \quad .$$

The function $H(s,s')$ gives the probability that the initial e^+e^- system with center-of-mass energy s has radiated one or several initial state photons, so that the remaining available energy for annihilation is s'. This function has been calculated up to second order in α_{em} with exponentiation of higher orders [22].

In equation 1.2, we have made no assumptions about the existence of the top quark or Higgs boson. The only model dependent part is that it uses SM calculation for the scale factor I_f of the $\gamma - Z$ interference term.[2]

In this model independent approach, instead of the SM parameters such as M_{top}, M_H, M_Z and $\alpha_s(M_Z^2)$, we will fit for the lineshape parameters such as Γ_Z, Γ_{ff}, σ^0_{ff}, and M_Z. It can be easily shown that it is equivalent to fit firstly the cross-sections to get the M_Z, Γ_Z and other lineshape parameters , and then fit the obtained electroweak parameters in the context of the SM to get the top quark mass, $\alpha_s(M_Z^2)$, or to some extent the Higgs mass.

[2]If instead the $\gamma - Z$ interference terms are entirely determined from the Z resonance cross section data, the error on M_Z is increased to 13 MeV, and the error on Γ_Z to 7 MeV.

1.4 Extraction of electroweak parameters

From previous discussion, by fitting the hadronic cross sections to equation 1.2, we can extract M_Z, Γ_Z, and σ_h^0. By taking the ALEPH results of leptonic cross section measurements, from the combined lineshape fit, we can get hadronic partial width Γ_{had}, and charged lepton partial widths Γ_l, $(l = e, \mu, \tau)$. In the SM, assuming lepton universality , the Z total width can be expressed as:

$$\Gamma_Z = \Gamma_{had} + 3\Gamma_l + \Gamma_{inv} \quad ,$$

where Γ_{inv} is the invisible width for Z decay into neutrinos, which go undetected. In the SM, $\Gamma_{inv} = N_\nu \Gamma_\nu$, where N_ν and Γ_ν represent the number of light neutrino generations ($m_\nu \leq M_Z/2$) and partial width of $Z \rightarrow \nu\bar{\nu}$ respectively. By taking the SM value of $\Gamma_\nu/\Gamma_l = 1.992 \pm 0.003$ [11], the number of light neutrino species can be obtained by using the formula:

$$N_\nu = (\frac{\Gamma_{inv}}{\Gamma_l})/(\frac{\Gamma_\nu}{\Gamma_l}) \, . \tag{1.3}$$

In the SM, one additional specie of light neutrinos would result in an increase of 6.6% in Z total width and decease of 13% in the peak cross sections. So the number of light neutrinos' measurement can effectively set a strong constraint on the SM. Figure 1.5 shows the SM predicted hadronic cross sections as center-of-mass energy with number of neutrino generations of 2, 3 and 4.

Lastly, since in the SM with radiative corrections, any Z resonance observ-

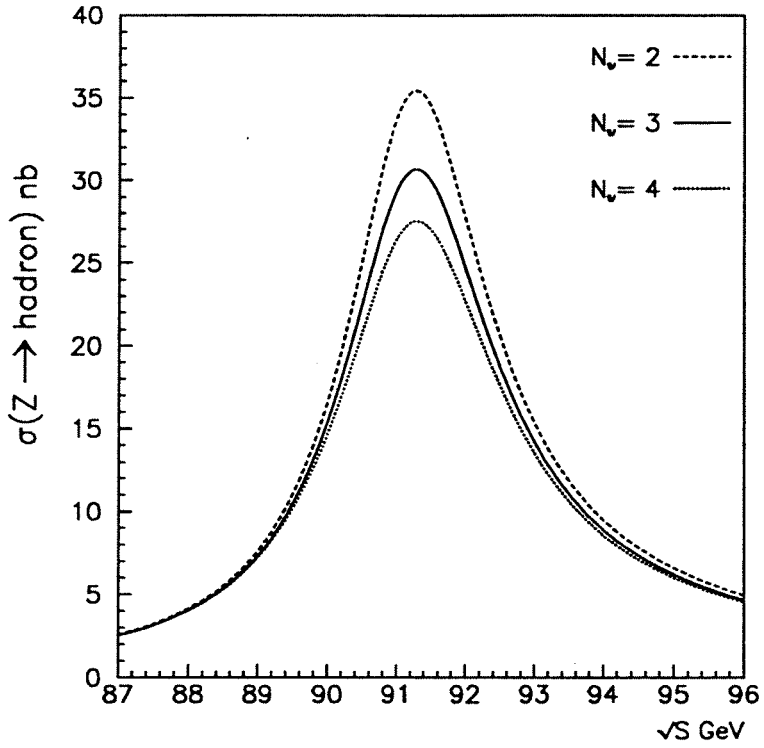

Figure 1.5: SM predicted hadronic cross sections as center-of-mass energy with number of neutrino generation of 2, 3 and 4.

ables can be parameterized as function of $\alpha_{em}, \alpha_{em}(M_Z^2), G_F, M_Z, M_{top}, M_H$, and $\alpha_s(M_Z^2)$, one can use the precisely measured physical lineshape parameters to constrain the less well known parameters M_{top}, M_H and α_s in the context of the SM. For instance, the Z resonance observable $R_l = \Gamma_{had}/\Gamma_l$, can be used to extract $\alpha_s(M_Z^2)$, since in the SM, R_l is simply related to $\alpha_s(M_Z^2)$ in a form [23]:

$$R_l = R_l^0 \left(1 + 1.06\frac{\alpha_s(M_Z^2)}{\pi} + (0.9 \pm 0.1)\left(\frac{\alpha_s(M_Z^2)}{\pi}\right)^2 - 15\left(\frac{\alpha_s(M_Z^2)}{\pi}\right)^3\right) , \tag{1.4}$$

where $R_l^0 = 19.943 \pm 0.030$ in the SM [24], calculated using $M_Z = 91.1887\ GeV$, $M_t = 175\ GeV$ and $M_H = 300\ GeV$. This determination of R_l is very clean theoretically, and a good test for QCD.

More importantly, the Z partial widths after the electroweak radiative corrections, gain a quadratic M_{top} dependence. So we can use Γ_Z and Γ_l measurements to constrain the top quark mass and to a less extent the Higgs mass[3] (the leading correction is logarithmic for Higgs mass.) For the other lineshape parameters such as σ_{had}^0 and R_l, the top mass dependence essentially cancels out.

[3]In this dissertation, due to the limited measurement precision, the fit to constrain the Higgs mass is not performed.

1.5 Sensitivity of σ_{ff} to M_Z and Γ_Z

To measure the Z lineshape, one has to decide at which energies one should measure the cross sections. For the peak cross section measurement, the best choice is at the energy point where cross section is maximum. To measure the Z mass and width, however, at least two additional energy points are required. One approach to find the additional best energy points is to build sensitivity functions of cross sections to M_Z and Γ_Z. They are calculated as shown below: for $\sigma_{ff}(W)$, the cross section measured at center-of-mass energy W ($W = \sqrt{s}$), the statistical error on Γ_Z can be written as:

$$\Delta\Gamma_Z = \left(\frac{d\sigma_{ff}(W)}{d\Gamma_Z}\right)^{-1} \Delta\sigma_{ff}(W) \; .$$

Here the error $\Delta\sigma_{ff}(W)$ is given by:

$$\Delta\sigma_{ff}(W) = \frac{\sigma_{ff}(W)}{\sqrt{N}} = \sqrt{\frac{\sigma_{ff}(W)}{\mathcal{L}}} \quad ,$$

where N is the accumulated number of $Z \to f\bar{f}$ events and $\mathcal{L}$ is the accumulated luminosity at energy point W.

Combining above two equations, we have:

$$\Delta\Gamma_Z = \frac{1}{\sqrt{\mathcal{L}}} \frac{1}{S(W,\Gamma_Z)} \quad ,$$

$$S(W,\Gamma_Z) \equiv \frac{1}{\sqrt{\sigma_{ff}(W)}} \frac{d\sigma_{ff}(W)}{d\Gamma_Z} \quad ,$$

where $S(W, \Gamma_Z)$ is the sensitivity function for the Γ_Z. In the same way, we can derive the sensitivity function for M_Z. For a given luminosity, one can see that the larger the sensitivity the smaller the error. Figure 1.6 shows the hadronic cross section sensitivity curves for M_Z and Γ_Z. From the curves, the most sensitive energy points for Z mass are around 90.3 GeV and 92.2 GeV (the so called peak−1 and peak+1 points). For the Γ_Z, the two most sensitive energy points are around 89.4 GeV and 93.2 GeV (so called peak−2 and peak+2 points). In 1993, LEP was running on the peak−2, peak, and peak+2 energies to optimize the Γ_Z measurement.

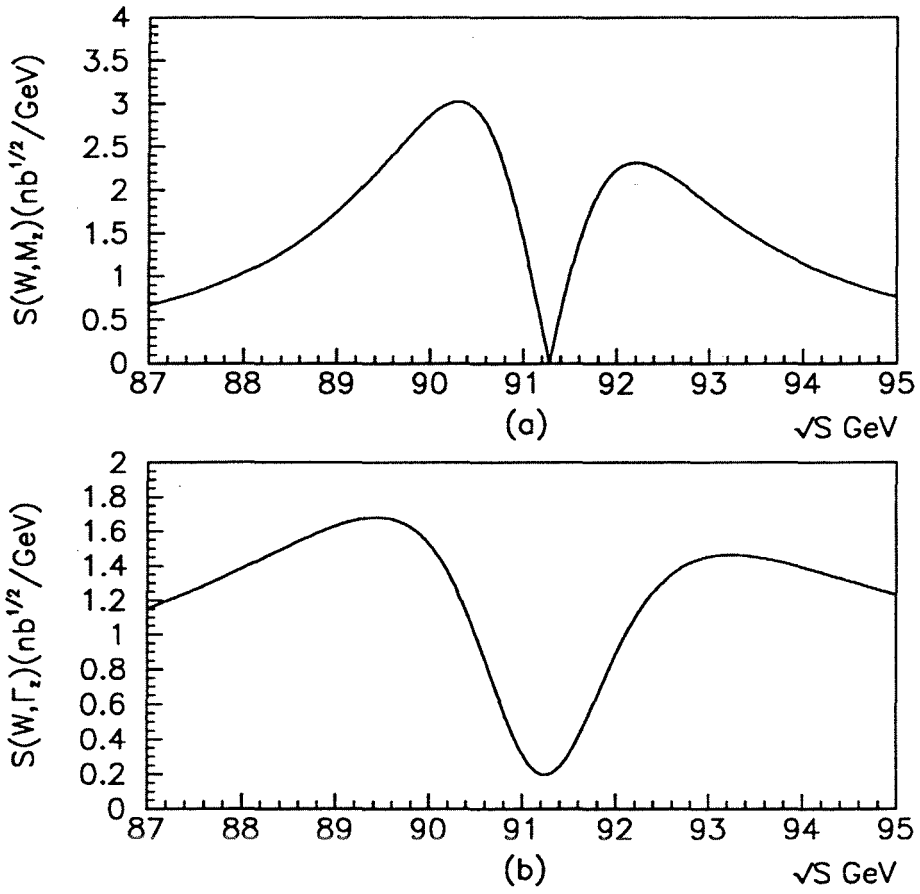

Figure 1.6: (a) Sensitivity function for M_Z. (b) Sensitivity function for Γ_Z.

Chapter 2

LEP and ALEPH

2.1 The LEP collider

2.1.1 The basic features of LEP

LEP, the Large Electron-Position Collider built at CERN [25] (European Laboratory for Particle Physics), Geneva, Switzerland lies in an underground tunnel at a depth of 40-150 meters. It is by far the largest operating machine in the world, with a circumference of 26.66 km, and a bending radius of 3.13 km in the magnets.

The LEP main ring has a total of 3304 dipole bending magnets, each of which has a peak magnetic field 0.135 T. There are at present 64 accelerating radio frequency cavities, each with a maximum power of 125 kw, which can accelerate the electron and positron beams up to 60 GeV. The energy radiated per turn in the LEP ring by an electron of 45.6 GeV is about 125 MeV.

Figure 2.1 shows the LEP injection chain composed of: the linac systems which accelerate electrons and positrons up to 600 MeV, a small Electron Positron Accumulator (EPA) to collect sufficient number of electrons and positrons to achieve the desired luminosity, a proton synchrotron (PS) to accelerate the beams to 3.5 GeV, and the Super Proton Synchrotron (SPS) to achieve 20 GeV. The current LEP beam dimensions at interaction points are:

- Horizontal $\sigma_x \approx 140\mu m$
- Vertical $\sigma_y \approx 3\mu m$
- Bunch length $\sigma_z = 0.7cm$

The luminosity of a collider machine is defined as:

$$\mathcal{L} = f_{rev} k \frac{N_+ N_-}{4\pi\sigma_x\sigma_y}$$

At LEP, the revolution frequency is $f_{rev} \simeq 11k$Hz, and the number of particles per bunch is $N_+ \simeq N_- \simeq 2\times10^{11}$ which corresponds to a beam current about 3.6 mA. Before September of 1992, the number of bunches was $k = 4$, and the maximum luminosity of LEP was around $10^{30}cm^{-2}sec^{-1}$. Since September 1992, LEP has been running with 8 bunches. In 1994, a LEP beam current of over 5 mA was achieved, giving a peak luminosity of $2.1 \times 10^{31}cm^{-2}sec^{-1}$. The average luminosity lifetime in the LEP machine is about 10 hours. There are four multi-purpose detectors (ALEPH, DELPHI, L3 and OPAL) taking data at LEP.

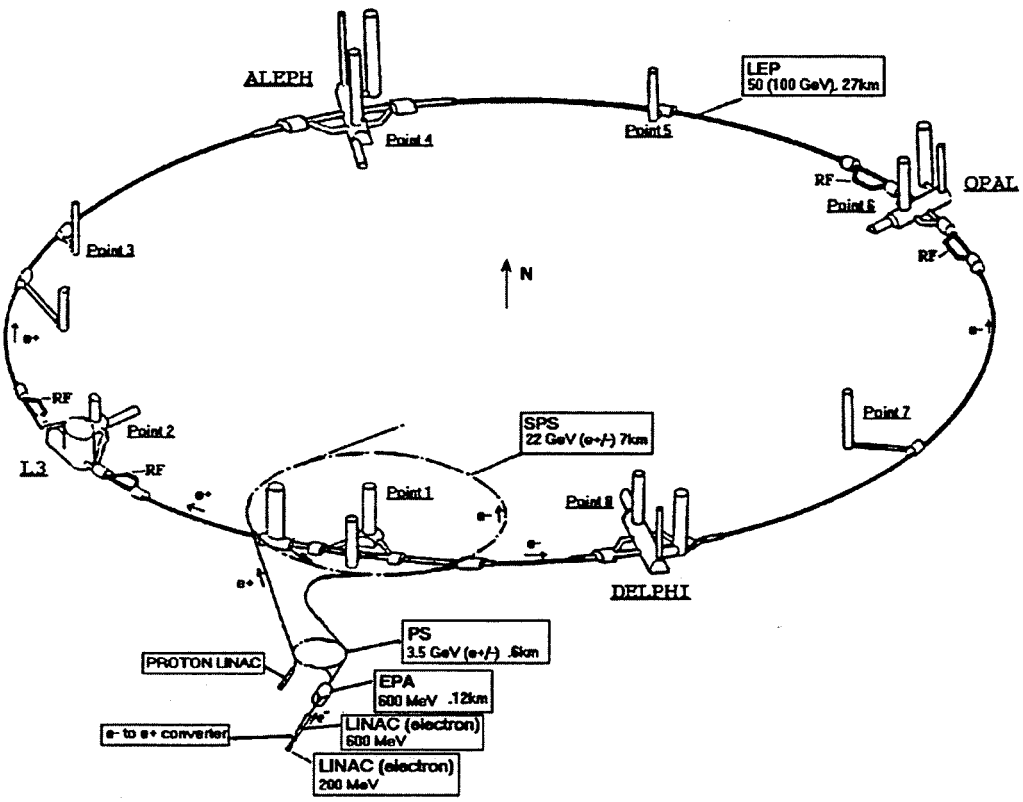

Figure 2.1: LEP ring and injection chains, and experimental zones.

2.1.2 LEP beam energy measurement

The LEP beam energy is defined by the integral bending magnetic field along the orbit. This field is measured from a reference dipole magnet [26] in series with the main ring bending magnets. Due to the iron and concrete structure of the main ring dipole magnet, the magnetic field measured in the reference magnet (made of iron only) has to be corrected for the time variations (aging) and temperature of the main ring magnets.

A more precise measurement of the LEP beam energy was obtained by measuring the rotation frequency of 20 GeV protons injected in LEP on the same orbit as positrons [27]: the difference in velocity is very accurately measured and the energy is known in terms of the proton mass. The relative precision of this method at 20 GeV is 10^{-4}. The determination of the beam energy at 45 GeV depends on extrapolations from the energy measurement at 20 GeV, this introduces an uncertainty about 20 MeV in the center-of-mass energy at the Z resonance.

Since 1991, LEP has been using the resonant depolarization method [28] to measure the beam energy. This method is based on the fact that in an e^+e^- storage ring, because of a small asymmetry in synchrotron radiation [29], the beam particles tend to be polarized in a direction parallel to the bending magnetic field. The beam energy is determined by measuring the frequency with which the spins of transversely polarized electrons precess about the vertical bending field. With this method, the precision of 10^{-5} is achieved. A detailed description of the LEP beam energy measurement using the resonant

depolarization method can be found in Appendix A.

In the 1993 LEP energy scan, the resonant depolarization method was frequently used to measure the beam energy at each of the off-peak scan points (89.4 GeV and 93.0 GeV). This has led to a significant reduction of the LEP beam energy errors and to the systematic errors on the M_Z and Γ_Z.

2.2 The ALEPH detector

ALEPH (Apparatus for LEP Physics) [30] is a large multi-purpose particle detector, built by a collaboration of over 30 institutes from Europe, the United States and China. The goal of the detector is to record in detail the results of e^+e^- collisions at center-of-mass energies up to 200 GeV. The detector was designed to have high granularity and good hermeticity around the beam interaction region.

The ALEPH detector is located at point 4 of the LEP ring about 150 meters underground at the foot of Jura mountains. A cut away view of the ALEPH detector is shown in Figure 2.2.

2.2.1 Tracking system

The tracking system, in order from inner to outer, consists of a Vertex Detector (VDET), an Inner Tracking Chamber (ITC) and a Time Projection Chamber (TPC).

The Vertex Detector

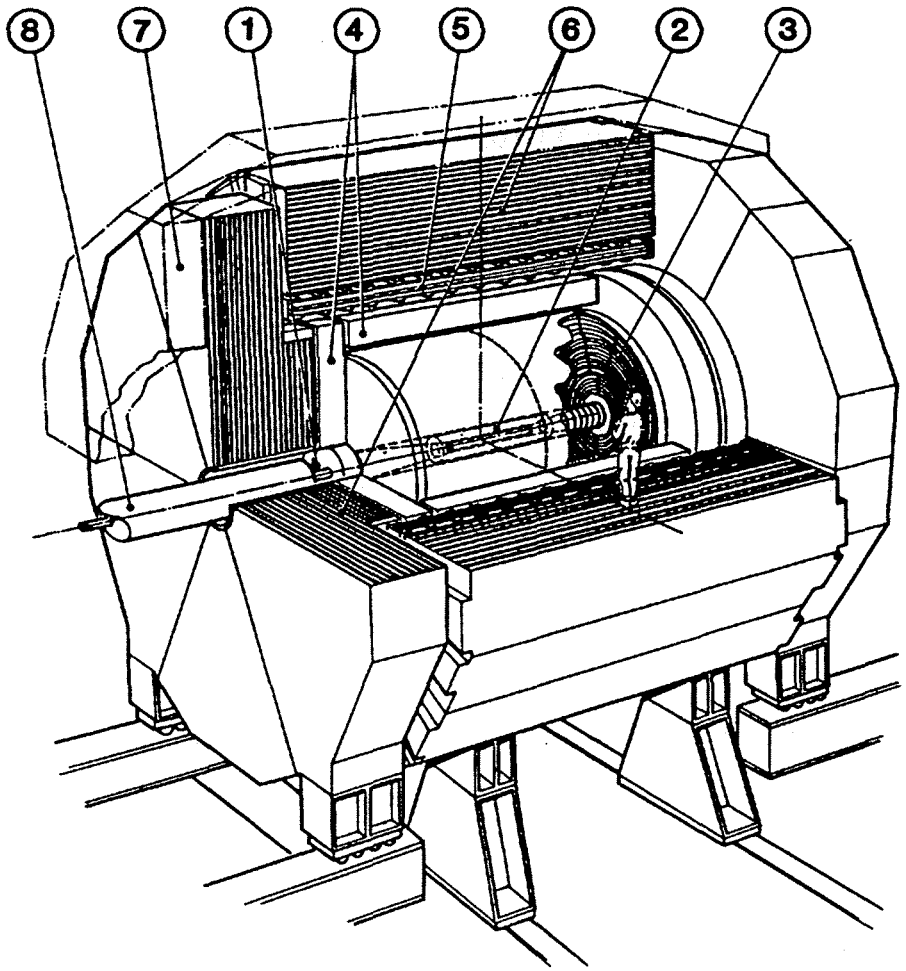

Figure 2.2: View of ALEPH. The labels indicate 1) Luminosity Calorimeter, 2) Inner Tracking Chamber, 3) Time Projection Chamber, 4) Electromagnetic Calorimeter, 5) magnet coil, 6) Hadron Calorimeter, 7) Muon Chambers, and 8) low-β quadrupole magnet.

Close to the interaction point, tracking is performed by a silicon microvertex detector (VDET) . This device consists of two coaxial layers of silicon wafers around the beam pipe. Each silicon wafer has 100 μm strip readout both parallel ($r\phi$) and perpendicular (rz) to the beam direction. For perpendicularly incident tracks, the VDET point resolution is $\sigma_{r\phi} = 12\mu m$, with $\sigma_Z = 10\mu m$. A detailed description of the vertex detector is given in Reference [32].

The Inner Tracking Chamber

The Inner Tracking Chamber (ITC) [33] is a conventional cylindrical drift chamber situated just outside of the VDET. It is operated at atmospheric pressure in an $Ar(80\%) + CO_2(20\%)$ gas mixture. The ITC has eight layers of signal wires, composed of 96 small staggered cells on the inner four layers and 144 on the outer four layers. It can provide up to 8 measurements of the $r\phi$ position of a track. The resolution depends on the drift length in the cell, with an average of $150\mu m$. With a total length of 2 meters, the ITC covers 97% of the solid angle.

The Time Projection Chamber

The ALEPH principle tracking device is a large Time Projection Chamber (TPC) [34]. A cut away view of the TPC is shown in Figure 2.3.

It has a large cylindrical drift volume filled with an $Ar(91\%) + CH_4(9\%)$ gas mixture. An uniform electric drift field (12.5kV/m) is built up by the high voltage (27000 V) central membrane, the inner and outer field cages and the planar wire chambers at the two end caps. For each TPC endcap, there

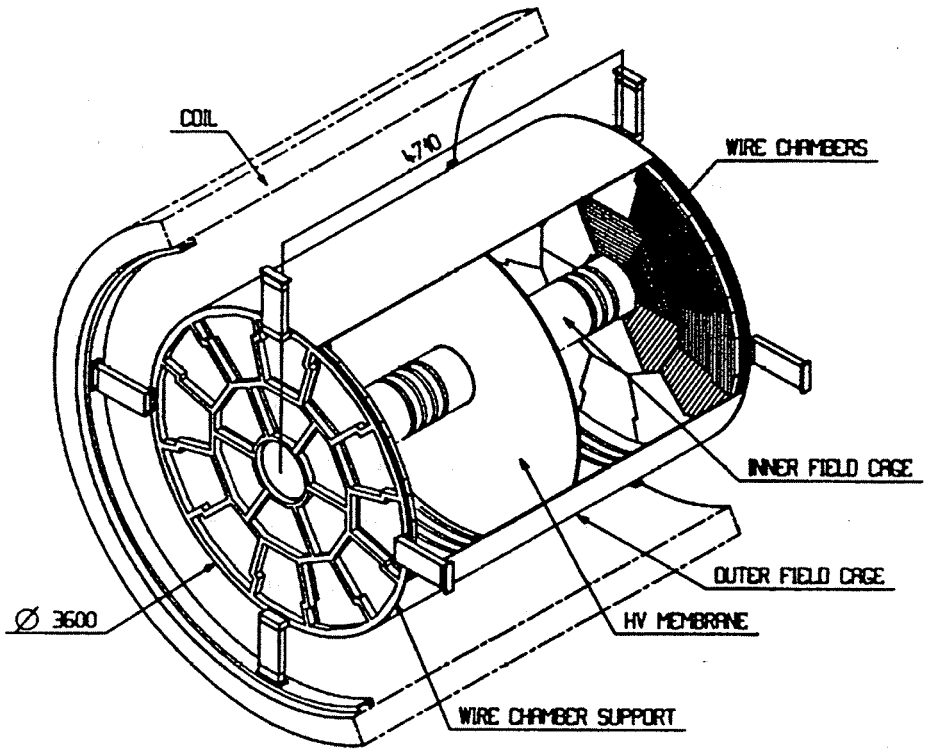

Figure 2.3: ALEPH TPC cut away view. The TPC inner radius is 0.31 m, outer radius is 1.8 m, and the drift length is 2×2.2 m.

are 6 inner sectors and 12 outer sectors. There are 9 concentric cathode pad rows and 148 wires for inner sectors and 12 pad rows and 196 wires for the outer sectors. With these the TPC can provide up to 21 three dimensional measurements for a charged track. The $r\phi$ information is obtained using the fired pads position, and the z coordinate information is provided by the drift time measurement.

The working process of the TPC can be described as follows: when a charged particle passes through the TPC, it produces an ionization trail in the gas. The electrons from the ionization are then driven to the endplates by the uniform electrical field. When the electrons reach the endcaps, a local avalanche on the sense wire occurs, the charges are recorded by the sense wires. At the same time, image charges are induced on the cathode pads below the fired sense wires. A TPC track is constructed by taking the following steps: firstly nearby hits are linked to form track segments, and then the segments are connected to form a track according to the helix hypothesis. Figure 2.4 shows the detailed wire and pad layout of a TPC sector.

The TPC single track resolution was measured from leptonic Z decays. It is $\sigma_{r\phi} = 180\ \mu m$, and $\sigma_z = 740\ \mu m$ for polar angle within 10^0. Both resolutions depend on the drift length and the orientation of the track relative to the pads and wires. The two-track separation capability is 15 mm in $r\phi$ and 20 mm in z. If we require at least 4 hits (TPC coordinates) for a good track measurement, the acceptance of the solid angle is 97%. The single-track finding efficiency is 98.6% for particles with momenta greater than 1 GeV/c

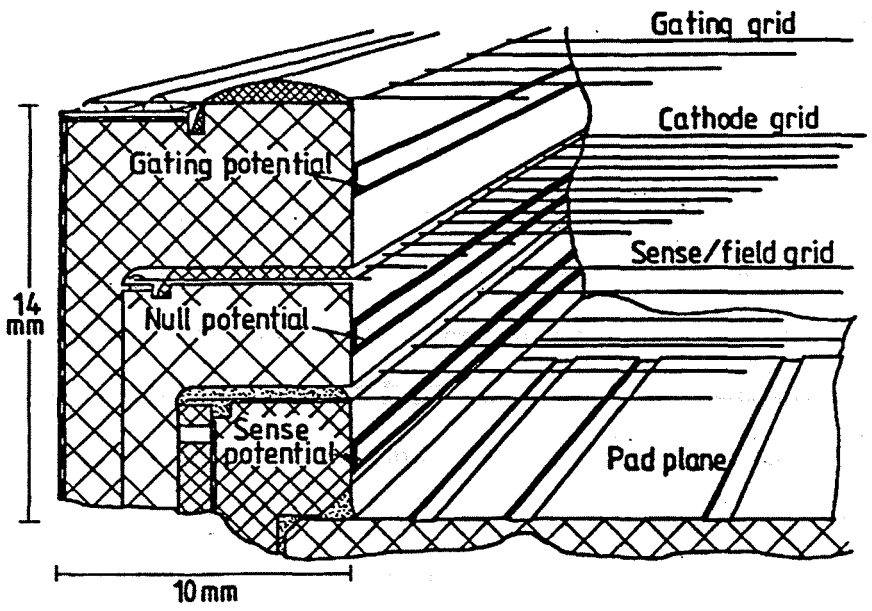

Figure 2.4: TPC sector wire plane and pad layout.

in jets at $\sqrt{s} = 91$ GeV (the efficiency for isolated tracks which cross all 21 pad rows is practically 100%). Since the TPC drift velocity is 5.2 $cm/\mu s$, the readout time for the TPC is about 42 μs. This is longer than the time interval of beam crossing ($11\mu s$ for 8 bunch beams), so the TPC is only used for the second level trigger.

In addition to providing the position measurements of charged tracks, the tracks' charge information recorded on the TPC sense wires can be used for dE/dx measurements. A maximum of 338 dE/dx measurements can be obtained for a charged track. The dE/dx resolution of the TPC for a well isolated track with 338 measurements is about 5% [35].

The Magnet

The magnet coil is a superconducting solenoid with helium cooled NbTi/Cu pipes surrounding an *Al* conductor. It provides a uniform 1.5 Tesla magnetic field parallel to the beam for the tracking chambers. In addition to providing the charged tracks' momentum measurement with the tracking chambers, the strong magnetic field is used to constrain the transverse diffusion of the drift electrons in the TPC. The magnet coil is situated outside of the electromagnetic calorimeter, and this has effectively reduced the materials in front of the calorimeter. The iron mass of the ALEPH hadron calorimeter serves as the field's return yoke.

2.2.2 Calorimeters

The energy measurements for electrons and photons are carried out by an Electromagnetic Calorimeter (ECAL). It is a sampling calorimeter made of lead sheets and wire chambers with a total thickness of 22 radiation length. A Hadron Calorimeter (HCAL) provides the energy measurements for strongly interacting particles. The HCAL is made of 23 layers of plastic streamer tubes separated by 5 cm thick iron slabs. With a total of 7.2 interaction lengths at 90 degree, the HCAL also serves as a filter for muons. In this dissertation, calorimeters are only used as trigger devices, a detailed description of the ECAL and the HCAL can be found in reference [30].

2.2.3 Luminosity monitors

At LEP the beam luminosity is measured by counting the rate of Bhabha events. Since September 1992, a solid-state luminosity calorimeter (SICAL) [36] has been used for the ALEPH luminosity measurement. It is a silicon-tungsten sampling calorimeter, which has 12 layers with a total thickness of 23.4 radiation length. Each layer is segmented into 16 annular pad rows in radius, the successive layers are rotated by 3.75^0 in ϕ to avoid aligned cracks between the layers. It is assembled from two sets of half-modules, and it is installed around the beam pipe with a distance from interaction point along the beam of 250 cm. The inner radius of the SICAL is 6.0 cm and outer radius is 14.6 cm. The polar angle coverage of the SICAL is from 24 to 58 *mrad*. Because the Bhabha scattering cross section increases with

the inverse square of the polar angle, the low angle coverage of the SICAL gains the statistical power in the luminosity measurement. A great effort was made to control the mechanical precision of the SICAL. The precision of the radial fiducial boundary uncertainty is kept smaller than $18\mu m$, leading to a luminosity experimental systematic error less than 0.1%. Details about the luminosity measurement with the SICAL will be discussed in section 3.1. The information about the ALEPH luminosity measurement before 1992 can be found in reference [37].

2.2.4 Trigger system

The trigger system [38] is designed to accept all genuine e^+e^- interactions. The redundancy of triggers enables about 100% efficiency for the real Z decays. For the hadronic Z decays, there are two main triggers:

- Energy deposits in the ECAL, requiring a total energy of 6.6 GeV deposited in the ECAL barrel, or 3.8 GeV in either endcap, or about 1.5 GeV in both endcaps.

- ITC-HCAL coincidence for penetrating charged particles, requiring track segments found in the ITC associated with the hits in a module of the HCAL in the same azimuthal region.

Since the ECAL energy trigger only uses energy and the ITC-HCAL trigger only uses the tracks, so these two triggers are mostly not correlated except very small correlations introduced by the geometrical acceptance of

the related subdetectors. The combined trigger efficiency is greater than 99.99% for the hadronic Z decays within the TPC acceptance.

Chapter 3

The Hadronic Cross Section Measurement

At LEP, electrons and positrons collide at center-of-mass energies around the Z pole and produce pairs of fermions:

$$e^+e^- \longrightarrow \gamma, Z \longrightarrow f\bar{f}$$

where $f\bar{f}$ can be a pair of quarks $q\bar{q}(u\bar{u}, d\bar{d}, s\bar{s}, c\bar{c}, b\bar{b})$ or a pair of leptons l^+l^- ($e^+e^-, \mu^+\mu^-, \tau^+\tau^-$ and neutrino pairs). According to the SM, approximately 70% Z decays are from $Z \rightarrow q\bar{q}$ and 10% Z decays are from processes $Z \rightarrow e^+e^-, \mu^+\mu^-, \tau^+\tau^-$. The rest are $Z \rightarrow \nu\bar{\nu}$; the ν's go undetected.

The hadronic cross section σ_{had} is measured by counting the number of

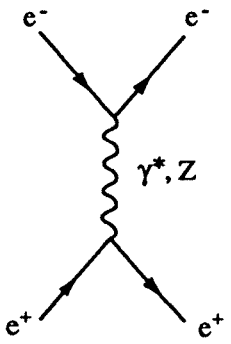

Figure 3.1: The lowest order Feynman diagram for the Bhabha scattering process $e^+e^- \rightarrow e^+e^-$. The diagram with the photon propagator is the dominant diagram in low angle Bhabha scattering. Diagram involving the Z as the propagator will provide corrections to the integrated cross section which are $\mathcal{O}(10^{-2})$ by two orders of magnitude.

hadronic events N_{had} in a given luminosity $\mathcal{L}$:

$$\sigma_{had} = \frac{N_{had}}{\mathcal{L}} \ .$$

In the following sections, we will first describe how the luminosity is determined and then give a detailed discussion on the hadronic event selection.

3.1 Luminosity determination

In e^+e^- collider experiments, Bhabha scattering provides an excellent means of measuring the absolute luminosity. As shown in Figure 3.1, the Bhabha event is an elastic scattering process of electrons and positrons.

The luminosity measured in the detector can be evaluated by the formula:

$$\mathcal{L} = \frac{N_{bhab}}{\sigma_{bhab}}$$

where N_{bhab} is the number of detected Bhabha events, and σ_{bhab} is the calculated cross section taking into account the luminosity monitor acceptance.

In theory, the Bhabha scattering is a well understood QED process. Its production cross section at small scattering angles is, at tree level:

$$\frac{d\sigma_0(s)}{d\Omega} = \frac{16\hbar c\alpha_{em}^2}{s}\frac{1}{\theta^4} \quad .$$

The integrated cross section between the minimum and maximum scattering angles θ_{min} and θ_{max} can be expressed as:

$$\sigma_0(s) = \frac{1040\ nb\ GeV^2}{s}(\frac{1}{\theta_{min}^2} - \frac{1}{\theta_{max}^2})$$

where s is the center-of-mass energy squared, and the polar angle θ is defined as deflection angle respect to the beam line in radians. From the formula, it is clear that in order to reduce the statistical errors, the Bhabha scattering detector must positioned as closely as possible to the beam line. For the SICAL, the minimum angle θ_{min} is 24 mrad and maximum angle θ_{max} is 58 mrad. Without considering the details of the acceptance and detector simulation, the calculated Bhabha cross section exceeds 100 nb. So the statistical precision will be better than 10^{-3} if more than $10pb^{-1}$ integrated luminosity is accumulated at each of the energy scan points. The uncertainty of the

Bhabha cross section is related to the precision of luminosity calorimeter boundaries in a form:

$$\frac{\Delta\sigma_{bhab}}{\sigma_{bhab}} \simeq 2 \times \frac{\Delta\theta_{min}}{\theta_{min}} \simeq 2 \times \frac{\Delta R}{R} .$$

Thus to match the statistical precision, a very good control for the mechanical precision of the detector boundaries is required. For the SICAL $R \simeq 6$ cm, the boundary position has to be know to a precision better than 30 μm to reach the experimental precision of 10^{-3}.

3.1.1 Bhabha event selection

Due to its elastic scattering nature, the Bhabha event is characterized as back-to-back e^- and e^+, each with the beam energy and scattered at very low angles. So the trigger for the Bhabha events can be designed based on the total energy deposited in each side of the SICAL. The ALEPH Bhabha triggers are composed of a single-arm high threshold trigger ($\sim$ 40 GeV), and double-arm low threshold trigger ($E_A > 12$ GeV).AND.($E_B > 24$ GeV) or ($E_B > 12$ GeV).AND.($E_A > 24$ GeV). Here E_A and E_B are the energies measured in the SICAL side A and side B respectively. The redundancy of having two triggers is that these two triggers's efficiencies can be cross checked against each other. The overall trigger efficiency for Bhabha events is measured to be near 100% within the SICAL acceptance [36].

For the Bhabha event selection, we can use the same idea as trigger designed by correlating the energy deposited by the electron and by the

positron in each side of the luminosity monitor. It requires:

- At least one shower cluster found in each side of the SICAL modules. The energy of the largest shower cluster on each side should be larger than 20 GeV.
- The sum of the energy of these shower clusters should be larger than 55 GeV.
- The largest shower of each side should satisfy a collinear requirement: $150° < \Delta\phi < 210°$.

A selected SICAL luminosity event is shown on Figure 3.2.

The background of the Bhabha event selection mainly comes from two sources. One is from the accidental coincidence of off-momentum beam particles. The off-momentum beam particles are those beam particles which lost part of their energy due to the collision with the residual molecules in the vacuum of the beam pipe. Near the detector, the focusing quadrupole magnetic field can deflect some of these off-momentum particles (electrons and positrons) to the luminosity calorimeter, and random coincidence of these beam particles provide a background for the Bhabha event sample. These background events usually have lower total energy than the Bhabha events. Also unlike the Bhabha pairs, the off-momentum beam particle pairs are not constrained to be collinear. After the Bhabha selection cuts, the remaining off-momentum beam particle background is estimated using a low threshold (9 GeV) single-arm trigger to be 0.07% of the Bhabha rate.

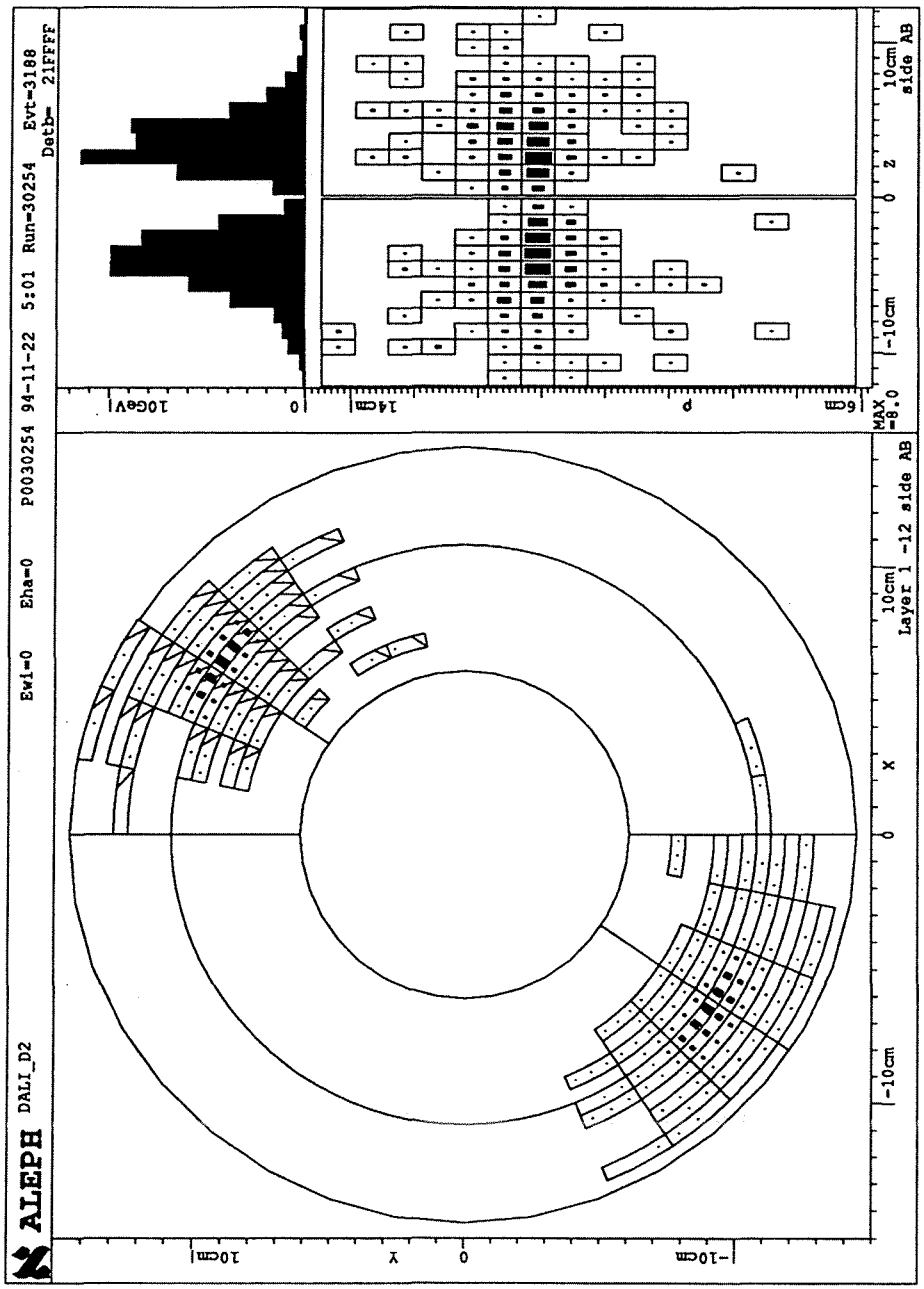

Figure 3.2: Typical Bhabha event in the SICAL. Clusters on A and B side are shown in the same view. The showers' z profiles are also shown from the interaction point toward $+Z$ or $-Z$; they are the sums of pads energies over $r-\phi$ for each side.

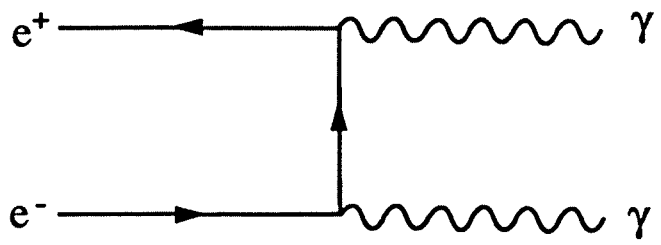

Figure 3.3: The t-channel two hard photon production Feynman diagram.

Another source of background is from the $e^+e^- \rightarrow \gamma\gamma$ process [39]. As shown in Figure 3.3, this process produces two or more hard photons, which can effectively simulate a pair of electrons and positrons in the SICAL. From Monte Carlo simulation, this background accounts for about 0.015% of the Bhabha event sample.

Figure 3.4 shows the energy correlation of the largest cluster on each side of the SICAL. The minimum energy requirements of the Bhabha event selection effectively remove most of the off-momentum beam background events. The collinear requirement of the two largest clusters of each side of the SICAL is aimed at reducing further the accidental coincidence of off-momentum beam particles. The $\Delta\phi$ distribution for the real data and Monte Carlo events (without background) is shown in Figure 3.5; the tails in the data distribution are used to estimated the background.

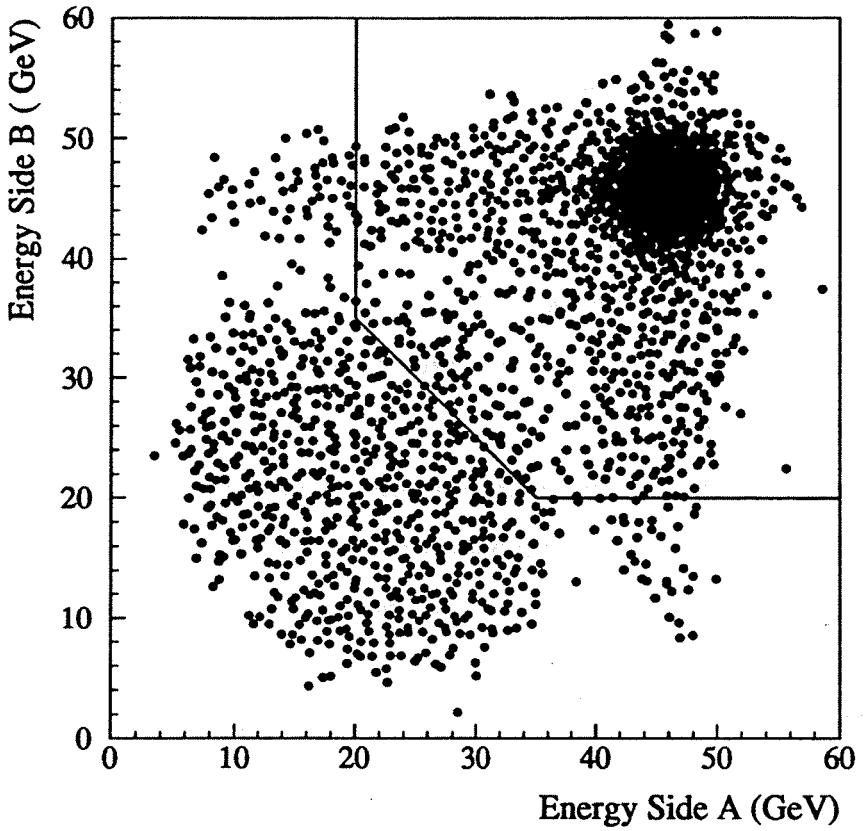

Figure 3.4: Largest reconstructed cluster energy on one side versus the largest reconstructed cluster energy on the other. The line indicates the cuts applied.

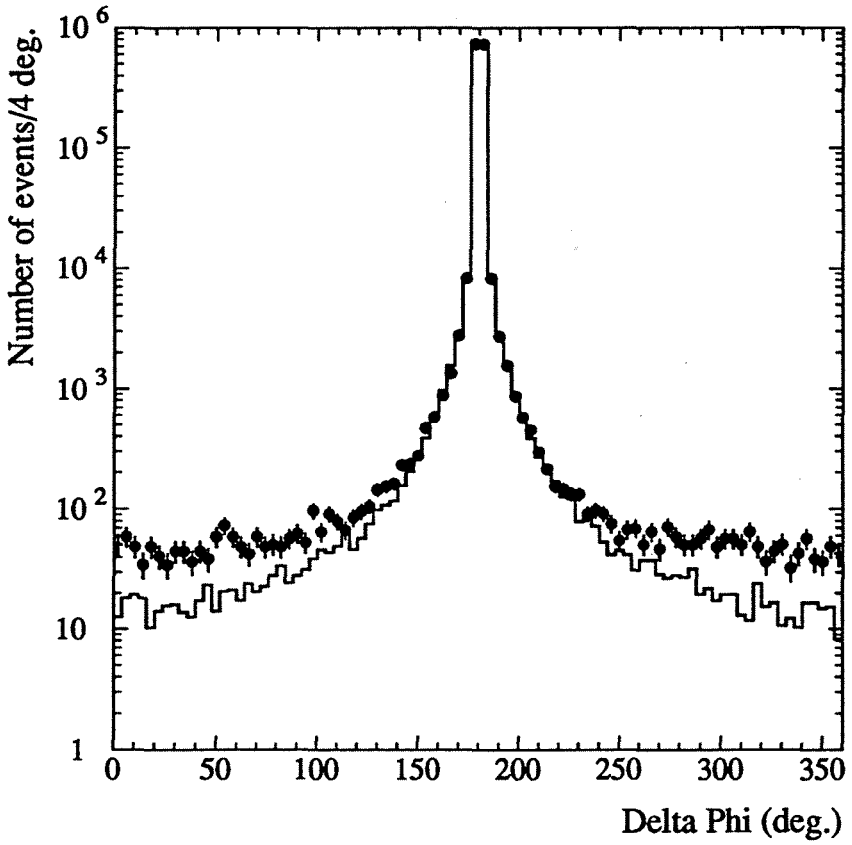

Figure 3.5: Distribution of the ϕ- difference $\Delta\phi$ between the each side of the clusters. Data are plotted as points and the Monte Carlo simulation (without background) is shown as a histogram.

3.1.2 Bhabha cross section and luminosity systematic errors

The Bhabha cross section for the SICAL is estimated by using a Monte Carlo program BHLUMI [40], which is a multi-photon $\mathcal{O}(\alpha^2)$ event generator. The cross section for the SICAL is determined by the formula:

$$\sigma_{sical} = \sigma_{theo} \cdot N_{acc}/N_{gen}$$

where N_{gen} is the number of generated events by BHLUMI, and σ_{theo} is the theoretical cross section calculated by BHLUMI with the SICAL acceptance. N_{acc} is the number of full detector simulated events accepted by the SICAL. The estimated cross section for the 1993 SICAL geometry and acceptance is about 84 nb. The uncertainties in this estimation are mainly from theoretical uncertainties in the σ_{theo} calculation due to the truncation of the higher order QED corrections. Currently, the error is estimated to be 0.16% [41].

For the luminosity measurement, beside the systematic errors from Bhabha cross section, another source of the systematic error is from the detector experimental errors. They are from the radial boundary uncertainties, the fidelity of the detector response simulation, and the Monte Carlo statistical errors. Table 3.1 [42] summarizes the systematic errors estimated in 1993.

Source of Uncertainty	1993 Estimation
Radial fiducial boundary	0.063%
Background estimation	0.011%
Simulation statistics	0.060%
Total experimental error	0.087%
Theoretical error	0.16%
TOTAL luminosity error	0.182%

Table 3.1: Summary of the SICAL 1993 luminosity systematic errors.

3.2 Hadronic cross section

Hadronic events at LEP have high multiplicity of final state particles and high visible energy. The measured charged multiplicity in hadronic events is about 21.3 ± 0.6 [43], and about 97% of hadronic events have charged energy more than 10 GeV. Figure 3.6 shows the end and side views of a typical hadronic event recorded in the detector.

3.2.1 Event selection

We can select hadronic events using cuts on the number of the tracks and charged energy. A hadronic event selection method based on charged tracks found in the TPC was developed [44]. It requires:

- At least 5 good charged tracks in the TPC
- The energy sum of the good charged tracks E_{chg} must be greater than 10% of the center-of-mass energy (assigning each track a pion mass)

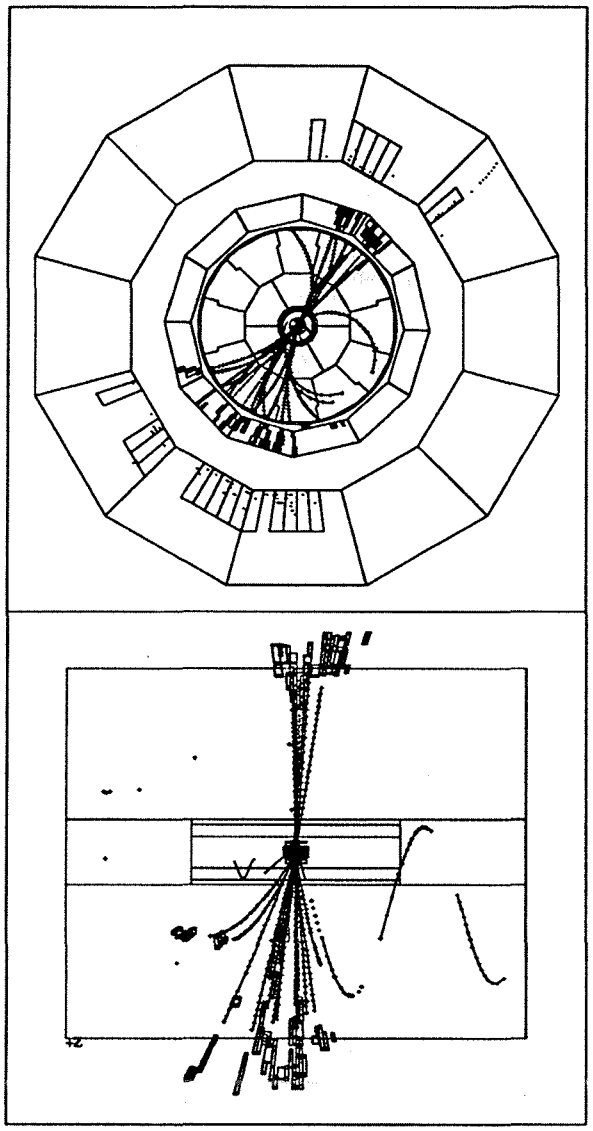

Figure 3.6: A typical hadronic Z decay in ALEPH shown in an endcap view (top) and side view (bottom) with only the ECAL and the TPC information displayed. The solid lines are the track fits to the ITC and the TPC coordinates (indicated by small '+'). ECAL energy tower is indicated by the small rectangular boxes. The HCAL energy tower is shown as large boxes and the end view shows strip hits tracing a muon's path through the iron.

Charged tracks are defined as "good" if the following conditions are satisfied:

- They must originate from a cylindrical zone of radius 2 cm and extending 10 cm on either side of the interaction point along the beam.
- They are required to have at least 4 TPC coordinates.
- They must satisfy $|cos\theta_{track}| \leq 0.95$
  where θ_{track} is the angle between the track and the e^+ beam direction.

The track origin requirements eliminate many poorly measured tracks, knock-on electrons, secondary arcs of low-momentum charged particles which loop inside the tracking detectors, tracks originating from secondary interactions and tracks from beam gas events.

The requirement of 4 TPC coordinates removes the most track fragments which usually do not have good tracking quality for the momentum measurement. The maximum dip angle requirement guarantees that a track crosses at least six TPC pad rows.

Most of the $Z \rightarrow e^+e^-$ and $Z \rightarrow \mu^+\mu^-$ events give only two charged tracks, and about 98% [4] of $Z \rightarrow \tau^+\tau^-$ events have less then 5 charged tracks. Therefore, the multiplicity requirement of 5 good charged tracks removes the most of $\tau^+\tau^-$ events and almost all e^+e^- and $\mu^+\mu^-$ events. The minimum track energy sum requirement removes most events produced from $e^+e^- \rightarrow e^+e^- + hadrons$ process (the so called "two-photon" events). Figure 3.7 shows a diagram of the two-photon processes. The final state electron and

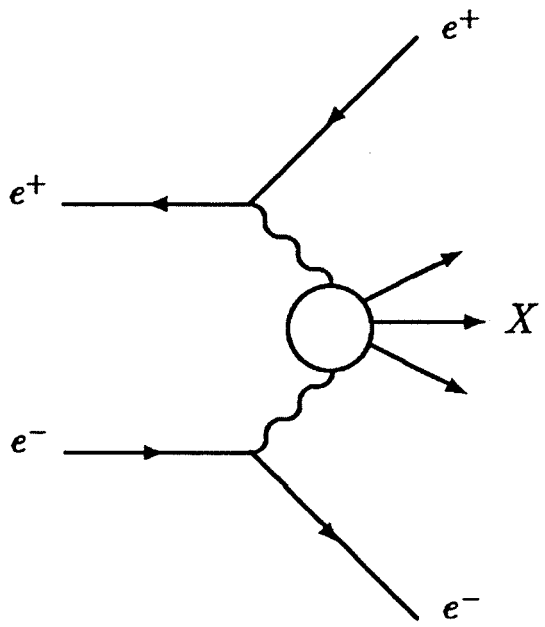

Figure 3.7: Diagram for the two-photon processes, $e^+e^- \rightarrow e^+e^- + hadrons$, which contributes to the low energy tails of the hadronic sample. The final state electron and positron often pass undetected down the beam pipe.

positron take most of the center-of-mass energy and are scattered in a very forward direction along the beam. As they often go undetected in the TPC, so the two-photon events usually have very low visible energy in the TPC tracking volume. At LEP, about 90% of two-photon event have visible energy less than 10 GeV. A more detailed study of the two-photon process can be found in reference [45]. Figure 3.8 shows a charged energy distribution of real data superimposed on the Monte Carlo predictions. The events in the plot have at least 5 good charged tracks.

3.2.2 Selection efficiency

The fully simulated hadronic Monte Carlo events from the process $e^+e^- \rightarrow Z, \gamma \rightarrow q\bar{q}$ at the peak energy are used to estimate the hadronic event selection efficiency. The efficiency is defined as:

$$\epsilon = \frac{\sigma(accepted)}{\sigma(\sqrt{s'} > \sqrt{s'_{min}})} \tag{3.1}$$

where s' is the invariant mass of the e^+e^- system after initial state radiation and $\sqrt{s'_{min}}$ is chosen to be 10% of $\sqrt{s}$. The selection efficiency calculated from 1993 Monte Carlo hadronic event generated at Z mass peak with full detector simulation is $(97.480 \pm 0.013)\%$. The error is Monte Carlo statistical only.

The hadronic event selection efficiency is not perfectly constant at the different energy scan points [46]. The 1993 data was collected mostly at

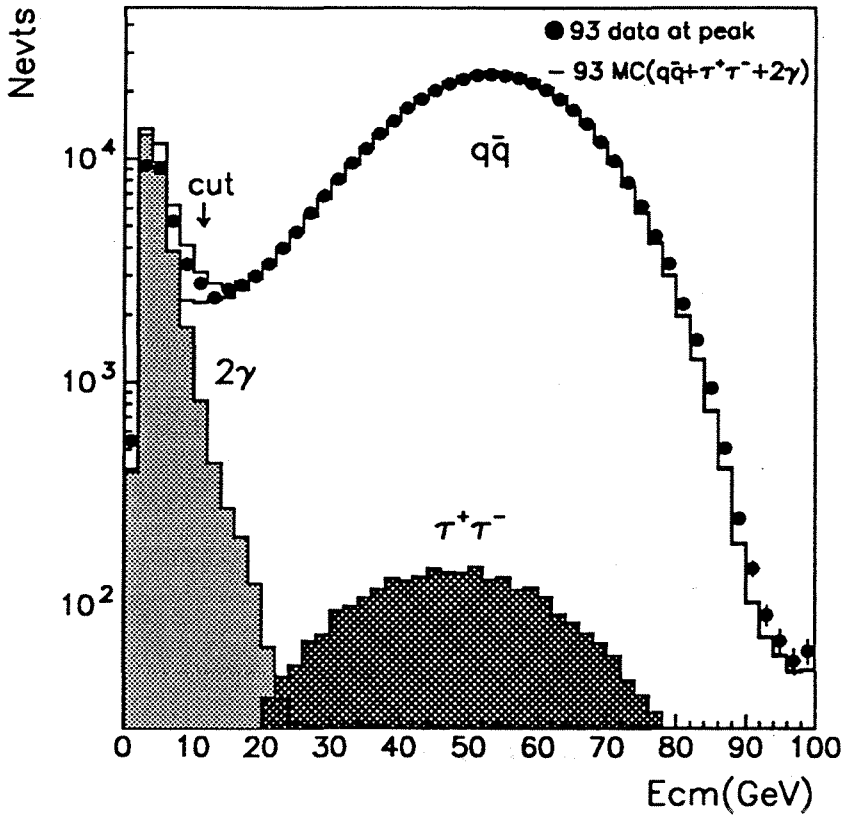

Figure 3.8: Distribution of charged energy with all contributions. More than five good charged tracks are required for the events in the histogram.

three energies, 89.4 GeV (peak−2), 91.2 (peak), and 93.0 GeV (peak+2). To estimate the selection efficiency at each of the energy points, a Monte Carlo study [46] was performed. Because the TPC tracking efficiency is very high, it can be modeled by applying very simple cuts at the generator level. It is enough to require five charged particles with $|cos\theta| < 0.95$ and energy sum larger than $0.1E_{cm}$ to well approximate the efficiency and study the relative changes between different energies. About 10 million such events were generated at each of the energy scan points using the ALEPH standard hadronic event generator HVFL04 [47] without detector simulation. By applying similar event selection cuts to these generated hadronic events, the efficiency at each of the energy points was calculated.

The hadronic event selection efficiency calculated in this way for each of the 1993 scan points is listed in Table 3.2. It also shows the efficiency

$\sqrt{s}$ (GeV)	89.4	91.2	93.0
$\epsilon(\sqrt{s})\%$	97.576 ± 0.005	97.603 ± 0.005	97.567 ± 0.005
$\epsilon(\sqrt{s}) - \epsilon(91.2)\%$	-0.027 ± 0.007	–	-0.036 ± 0.007

Table 3.2: Hadronic event selection efficiency as a function of $\sqrt{s}$, from generated hadronic events without detector simulation.

difference between the peak and off peak points. The uncertainties in the table are from Monte Carlo statistics only. The effect of this small efficiency difference is to shift up the Z width by about 1 MeV. In the efficiency calculation for the 1993 energy points, we use the efficiency calculated at peak ($97.480\% \pm 0.013\%$) as a reference, and use linear interpolation between the

energies in Table 3.2 to find the corrections to the selection efficiency at the luminosity-weighted average scan point energies. The calculated efficiencies for 1993 energy points is shown in Table 3.3.

Designation	*peak*-2	*peak*	*pre-scan*	*peak* + 2
Avg. $\sqrt{s}$ (GeV)	89.434	91.192	91.290	93.016
$\epsilon(\sqrt{s})$ %	97.454	97.480	97.478	97.443

Table 3.3: Hadronic event selection efficiency as a function of $\sqrt{s}$, used in 1993 hadronic cross section measurement.

Figure 3.9 shows the calculated relative efficiency difference between the Z mass peak point and the off peak points scanned at LEP between 1989 and 1993. Also shown is a plot of relative efficiency differences calculated with the events generated without initial state radiation. From the plot, it is clear that without initial state radiation, the efficiency is constant.

3.2.3 Background

The background in the hadronic event selection are mainly from $Z \to \tau^+\tau^-$ and two-photon processes. According to Monte Carlo simulation, about 93.30% of tau pairs are rejected by the hadronic event selection cuts. Taking the measured $Z \to q\bar{q}$ to $Z \to \tau^+\tau^-$ ratio 20.798 ± 0.066 [11], the estimated background contamination from tau pairs in the hadronic sample is 0.32%. It should be noticed that since τ production follows the same resonant behavior as hadrons, this background has no effect on the Z width measurements.

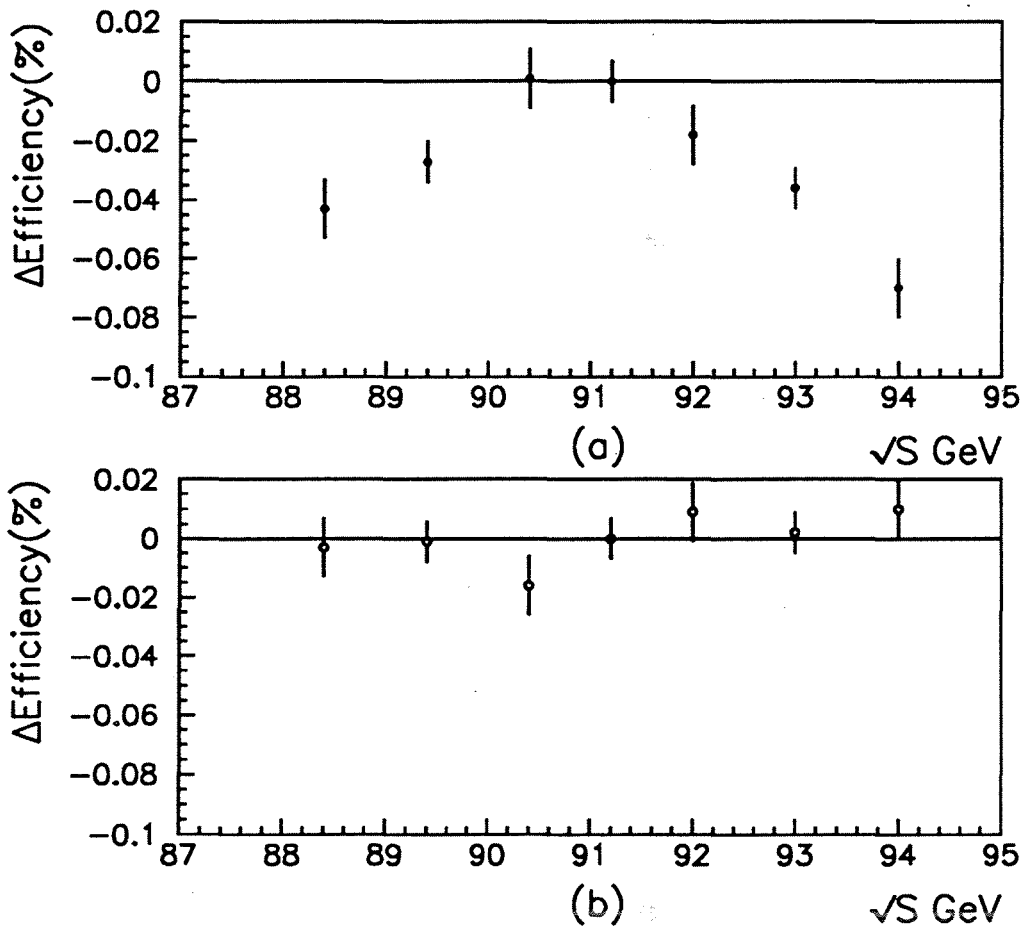

Figure 3.9: Monte Carlo hadronic event selection efficiency change as function of LEP center-of-mass energy: (a) with initial state radiation, (b) without initial state radiation. The peak efficiency change is chosen as the zero value of both plots.

The background from two-photon process is however hard to estimate accurately from Monte Carlo simulation. The current models for the two-photon processes are still under development and the experimental results have large errors [45]. As shown in Figure 3.8, the deviations between data and Monte Carlo are significant. In ALEPH the two photon background has been measured with the data by exploiting the different center-of-mass energy dependence of the two-photon background and hadronic Z decays. The cross section of the two photon process rises only logarithmically with center-of-mass energy, so we can treat it as constant across the Z resonance.

We measure the correlation between the cross section in the range $0.1 < E_{chg}/\sqrt{s} < 0.3$ where background from the two-photon process is expected and the cross section for events with $E_{chg}/\sqrt{s} > 0.3$ where the expected background is negligible [48]. For convenience of discussion, we define variables:

$$\sigma_L = \sigma(0.1 < E_{chg}/\sqrt{s} < 0.3) = \sigma_L^Z(\sqrt{s}) + \sigma_{\gamma\gamma}$$

$$\sigma_H = \sigma(0.3 < E_{chg}/\sqrt{s}) = \sigma_H^Z(\sqrt{s})$$

where σ_H^Z and σ_L^Z represent the resonant part of measured hadronic cross sections in the region of $0.1 < E_{chg}/\sqrt{s} < 0.3$ and $E_{chg}/\sqrt{s} > 0.3$ respectively. $\sigma_{\gamma\gamma}$ is the two photon cross section across the Z resonance region. Figure 3.10 shows a $E_{chg}/\sqrt{s}$ distribution of selected hadronic events from 1993 data collected at the peak energy point.

Since the cross section of the two-photon processes is constant across the

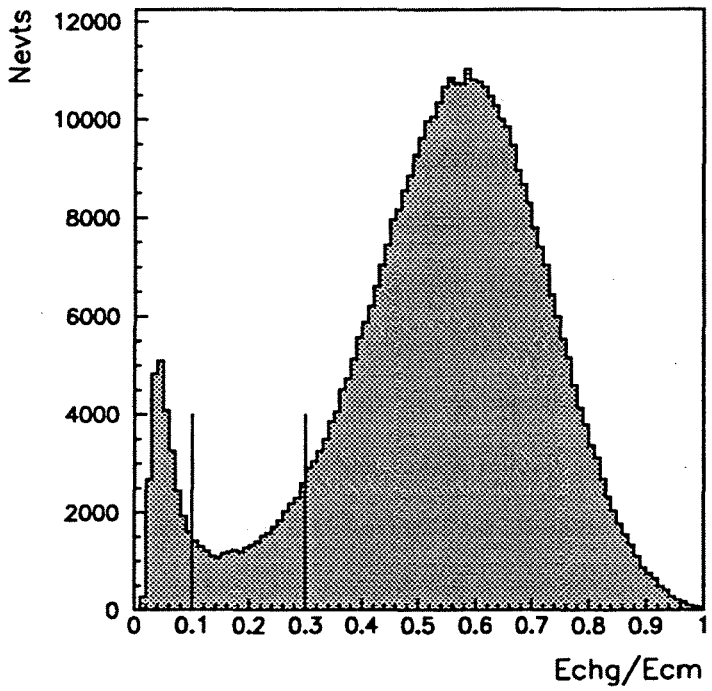

Figure 3.10: Normalized charged energy ($E_{chg}/\sqrt{s}$) distribution for 1993 peak scan data. All events in the plot have at least five good charged tracks. The two regions $0.1 < E_{chg}/\sqrt{s} < 0.3$ and $E_{chg}/\sqrt{s} > 0.3$ are divided by the vertical lines.

Z resonant region, by assuming the shape of the normalized charged energy distributions of hadronic events are the same for different energy point across the Z resonance, we can express the σ_L in a form:

$$\sigma_L = F\sigma_H + \sigma_{\gamma\gamma}$$

where $F = \sigma_L^Z/\sigma_H^Z$ and it is independent of energy points. By plotting the points (σ_H, σ_L) for each energy scan points across the Z resonance, we see that the resonant portion of the measured hadronic cross section will cause the points to lie on a straight line whose slope is the ratio of $F = \sigma_L^Z/\sigma_H^Z$. The nonresonant two-photon portion should cause the line to be shifted upwards. So we can perform a linear χ^2 fit to the plotted points of different energy scan points to extract the two-photon cross section. Figure 3.11 shows a plot of measured cross sections σ_H, σ_L from all the energy scan points from 1991 to 1993. The two-photon cross section estimated from the linear χ^2 fit is (93 ± 12) *pb*.

Notice that this value is obtained by assuming that the shape of the energy spectrum does not depend on scan energy points. In practice, this assumption is only a good approximation. For data collected in 1993 as shown in Figure 3.12, a small difference is observed between the off-peak energy spectrum (here peak+2 energy point is chosen) and peak energy spectrum. A Monte Carlo study shows this small difference is caused by the initial state radiation(ISR), and it has considerable effect on the Z width determination. Figure 3.13 and Figure 3.14 show the Monte Carlo simulated energy spectra

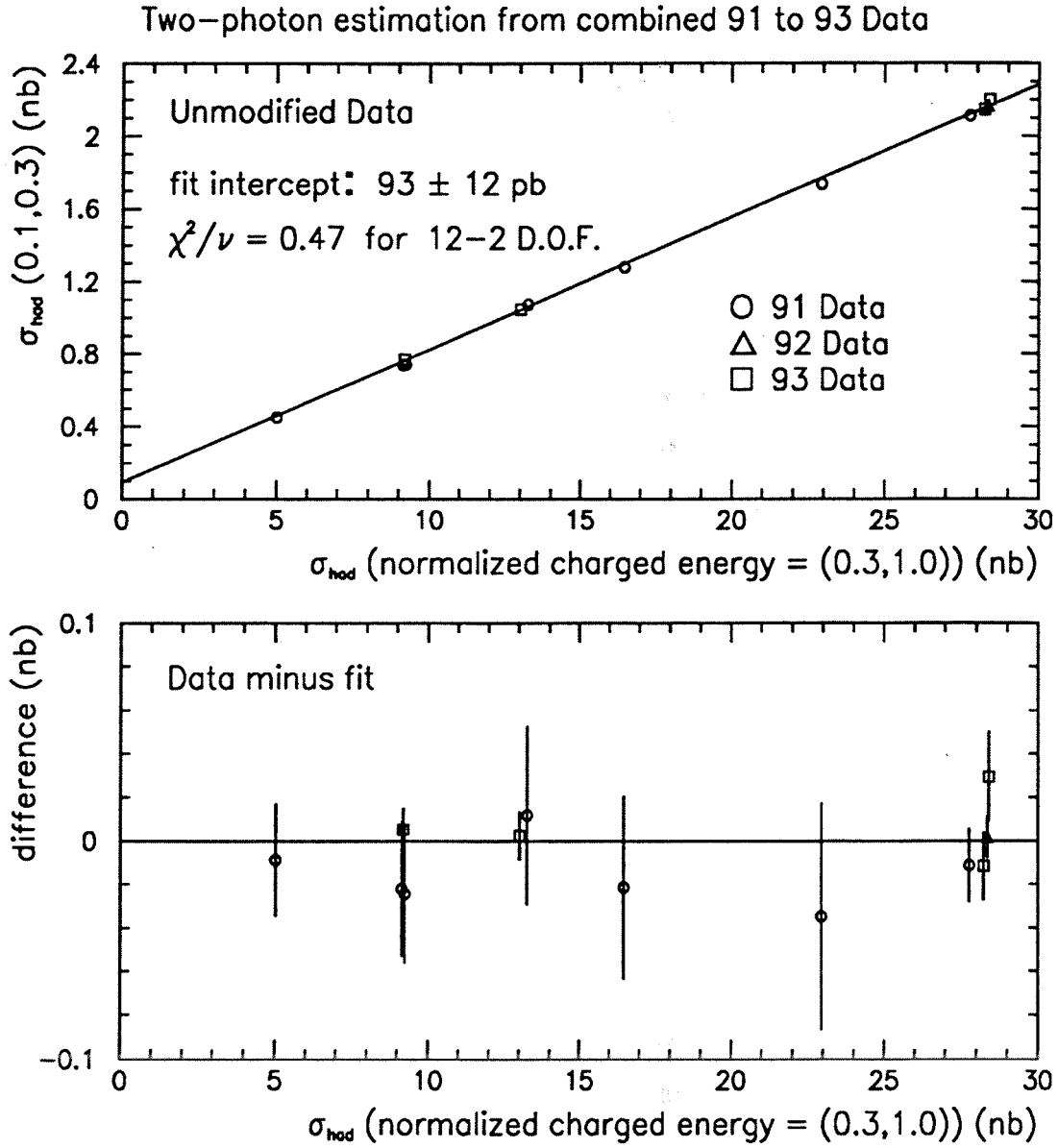

Figure 3.11: TPC hadronic selection: Nonresonant two-photon background estimation from 1991 to 1993 data without any corrections.

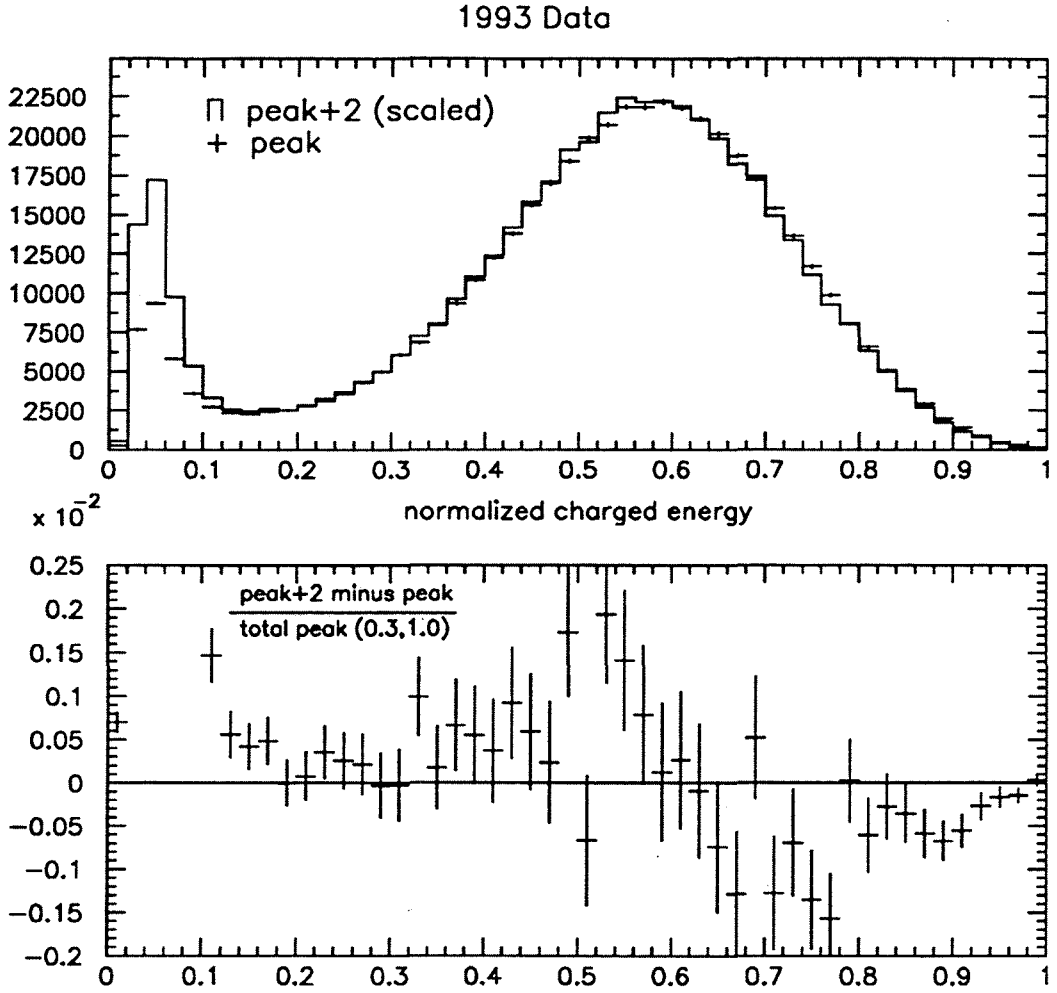

Figure 3.12: Normalized charged energy distributions for *peak* + 2 and *peak* data. All events in the plot have at least five good charged tracks. The *peak* + 2 distribution is scaled to have the same area as the *peak* distribution in the (0.3,1.0) region. The difference plot below is normalized to the number of *peak* events in the (0.3,1.0) region.

both with and without ISR.

To correct for the ISR effect in the energy spectrum, about 3 million Monte Carlo event have been generated at each of the scan points both with and without ISR, again without full detector simulation but with the simple selection cuts at the generator level. For each of the energy scan points in the Monte Carlo sample, the event count differences δN between with ISR and without ISR in the $(0.1 < E_{chg}/\sqrt{s} < 0.3)$ and $(0.3 < E_{chg}/\sqrt{s})$ energy regions are calculated by:

$$\delta N^{norm}_{(0.1,0.3)}(\sqrt{s}) = \frac{N^{withoutISR}_{(0.1,0.3)}(\sqrt{s}) - N^{withISR}_{(0.1,0.3)}(\sqrt{s})}{N^{withISR}_{(0.3,1.0)}(\sqrt{s})}$$

$$\delta N^{norm}_{(0.3,1.0)}(\sqrt{s}) = \frac{N^{withoutISR}_{(0.3,1.0)}(\sqrt{s}) - N^{withISR}_{(0.3,1.0)}(\sqrt{s})}{N^{withISR}_{(0.3,1.0)}(\sqrt{s})}$$

Here the δN values are normalized by the number of events in the high energy region , and represent the fraction of σ_H which must be added to or subtracted from σ_L and σ_H in the data to imitate the effect of removing the ISR. The δN values we obtain from the Monte Carlo calculation for some energy points scanned at LEP between 1989 and 1993 are listed in Table 3.4 with statistical uncertainties.

By applying the Monte Carlo calculated δN values to the data, the ISR effect corrected two-photon cross section estimated from 1991 to 1993 data is 81 ± 12 pb. The error is statistical only. Comparing with the previously estimated two-photon cross section of 93 pb, the ISR effect caused an over-estimate 12 pb of two-photon cross section. For 1993 hadronic cross section

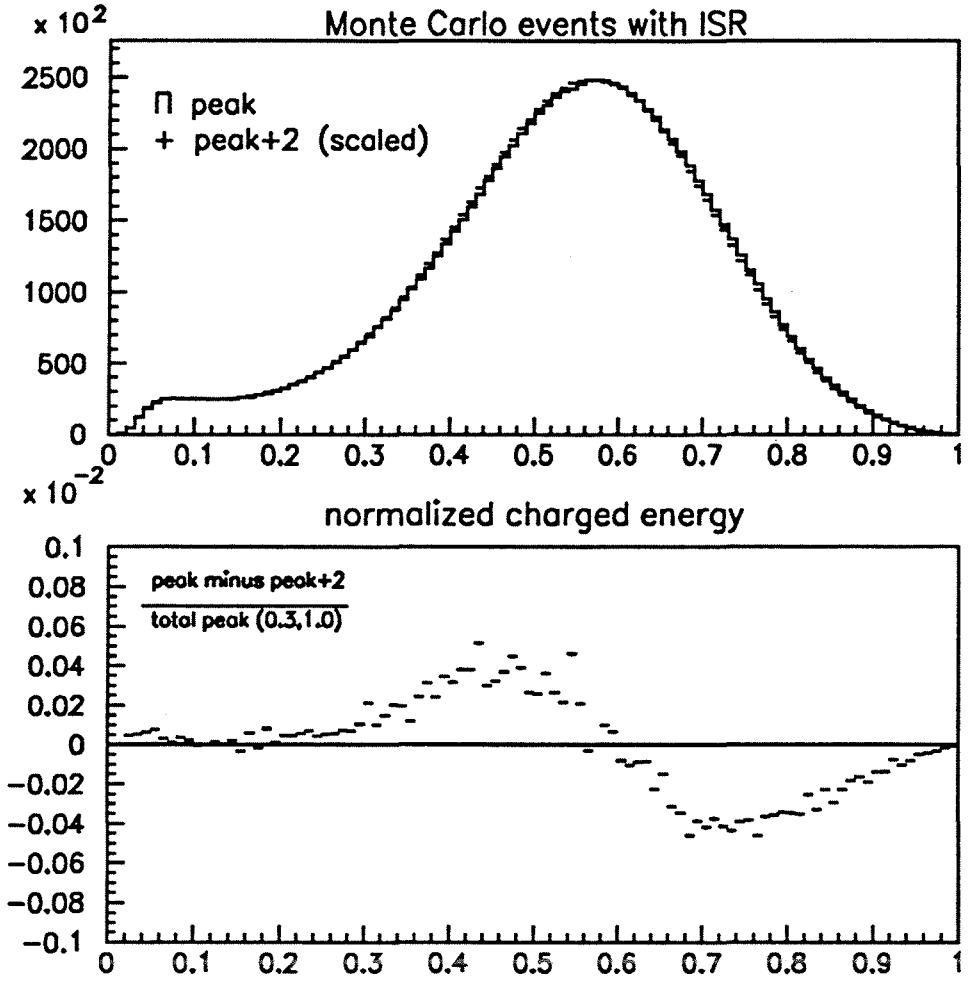

Figure 3.13: Normalized charged energy distributions for $peak + 2$ and $peak$ Monte Carlo, with ISR. All events in the plot have at least five generated charged particles.

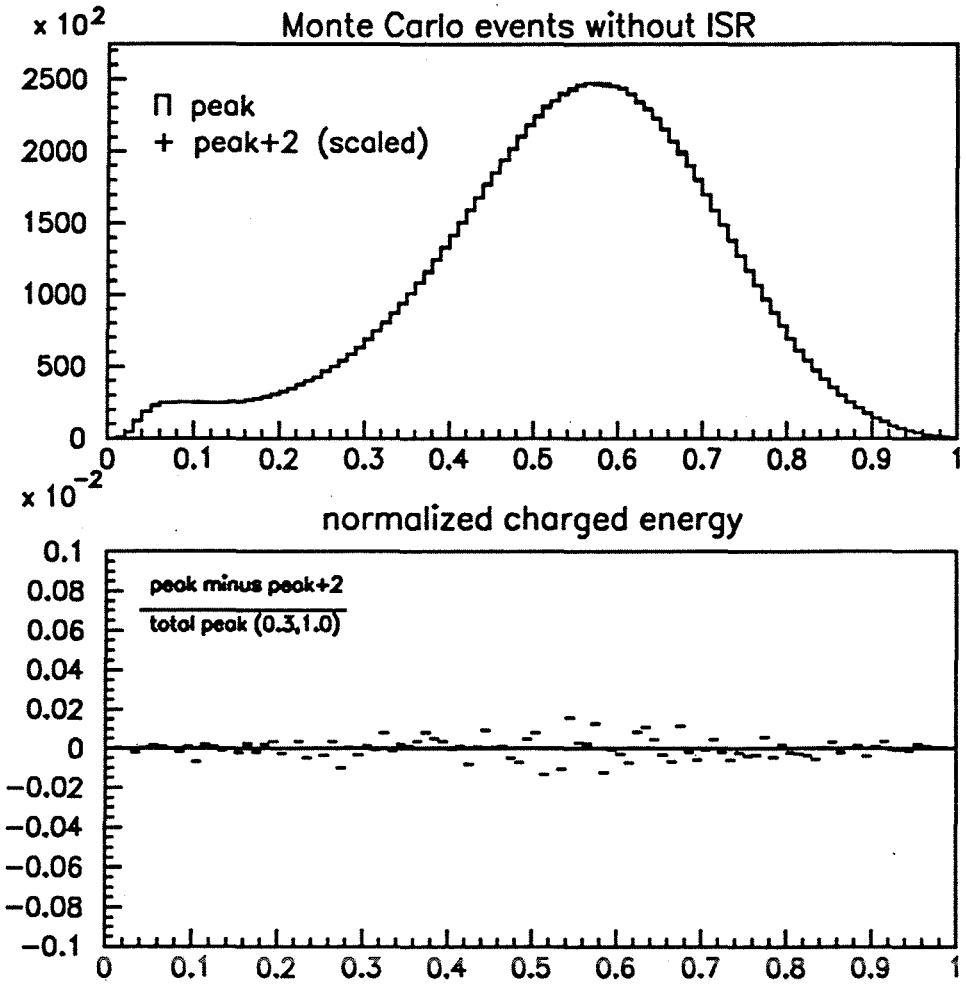

Figure 3.14: Normalized charged energy distributions for $peak + 2$ and $peak$ Monte Carlo, without ISR. All events in the plot have at least five generated charged particles.

$\sqrt{s}$ (GeV)	88.4	89.4	90.4	91.2	92.0	93.0	94.0
$\delta N^{norm}_{(0.1,0.3)}(\sqrt{s})$	-2.04	-1.06	-0.79	-0.70	-1.23	-1.66	-2.60
$* 10^{-3}$	± 0.24	± 0.13	± 0.23	± 0.13	± 0.23	± 0.13	± 0.24
$\delta N^{norm}_{(0.3,1.0)}(\sqrt{s})$	$+5.93$	$+3.09$	$+1.40$	$+1.25$	$+2.22$	$+3.21$	$+5.28$
$* 10^{-3}$	± 0.27	± 0.15	± 0.27	± 0.15	± 0.27	± 0.15	± 0.27

Table 3.4: δN values as a function of $\sqrt{s}$, calculated from Monte Carlo.

measurement, the effect of this correction shifts Z width up by about 1.5 MeV, which is about the same size as the LEP energy uncertainty on the Z width.

3.2.4 Cross section determination and uncertainties

The hadronic cross section for scan energy point i is given by:

$$\sigma^i_{had} = N^i_{had}/\mathcal{L}^i \quad .$$

Here N^i_{had} is the acceptance and background corrected number of hadronic events at scan energy point i:

$$N^i_{had} = \frac{1-\epsilon_\tau}{\epsilon^i_{acc}} N^i_{obs} - \sigma_{\gamma\gamma}\mathcal{L}^i$$

where N^i_{obs}, ϵ^i_{acc} and $\mathcal{L}^i$ correspond to the number of selected hadronic events, acceptance, and integrated luminosity at energy scan points i respectively. ϵ_τ is the estimated relative $\tau^+\tau^-$ contamination and $\sigma_{\gamma\gamma}$ is the measured

two-photon cross section.

The statistical uncertainty on the cross section at each energy scan point i is:

$$\Delta\sigma^i_{stat} \simeq \sigma^i_{had}\sqrt{\frac{1}{N^i_{obs}} + \frac{1}{N^i_{bhab}}} \ .$$

Table 3.5 lists the hadronic cross sections for each energy scan point along with the luminosity, number of observed events, efficiency, and background subtraction with their statistical errors.

$\sqrt{s}$ (GeV)	91.290	89.434	93.016	91.190
N_{obs}	160126	78774	119910	272279
ϵ_{acc}	97.478%	97.454%	97.443%	91.480%
$\mathcal{L}(nb^{-1})$	5331.8	8064.9	8692.6	9130.9
N_{bhab}	448583	707157	702292	769474
$\mathcal{L} * \sigma_{\gamma\gamma}$	432	653	704	740
ϵ_τ	0.32%	0.32%	0.32%	0.32%
σ_{had} (nb)	30.625 ± 0.087	9.907 ± 0.038	14.027 ± 0.044	30.407 ± 0.069

Table 3.5: Cross sections measured with the TPC hadronic event selection in 1993. The errors are statistical only.

The systematic errors on the hadronic cross section are mainly from two sources: the event selection acceptance estimation which depends on the Monte Carlo simulation, and the two-photon background estimation. The first of these two uncertainties was estimated by selecting real data events for which the thrust axis was nearly normal to the beam direction ($|cos_{thrust}| < 0.2$). These events were then rotate these events randomly in space and the tracks falling outside the detector acceptance were eliminated.

The efficiency was then recalculated by weighting the events passing the hadronic event selection with proper thrust angular distribution. This procedure was repeated for fully simulated 1993 Monte Carlo events. A recent study [49] showed a calculated efficiency difference of $(0.06 \pm 0.02)\%$ between Monte Carlo and data. Combining with all the uncertainties in the above procedure (detector response, Monte Carlo statistics, absence of low multiplicity events etc.), The total systematic error in the efficiency calculation is estimated to be 0.07% and this error is correlated between the 1993 energy scan points. The two-photon background uncertainty, as was discussed before, comes from the statistical error of the fit, and the uncertainty of 12 pb is common to all the 1993 energy points.

Table 3.6 summarizes the contributions of all 1993 systematic errors of the hadronic cross section measurements.

$\sqrt{s}$ (GeV)	91.290	89.434	93.016	91.190
Efficiency	0.07%	0.07%	0.07%	0.07%
$\tau^+\tau^-$	0.03%	0.03%	0.03%	0.03%
Two-photon (12pb)	0.04%	0.12%	0.09%	0.04%
Total	0.09%	0.14%	0.12%	0.09%

Table 3.6: Compilation of relative systematic errors of the 1993 hadronic cross section measurement, based on the TPC hadronic event selection, at each of the energy scan points.

Chapter 4

Z Lineshape Fit and Results

Using the hadronic cross sections measured at each of the energy scan points, we can perform a fit to obtain the Z resonance parameters M_Z, Γ_Z, and σ^0_{had}. In this chapter, we will first introduce the error matrix used in the Z lineshape fit, then the hadronic lineshape results, and finally the combined results with the ALEPH leptonic cross section measurements. Finally we will discuss the implications of the measured Z resonance parameters for the Standard Model (SM).

4.1 The fitting error matrix

In the Z lineshape fit there are two main sources of uncertainty which need to be considered: uncertainties in the cross section measurements, and uncertainties in the center-of-mass energies.

We used a χ^2 minimization algorithm to extract the Z lineshape pa-

rameters. Considering possible correlations between systematic errors in the cross section measurements, and LEP beam energy correlations between scan points, we define the χ^2 as:

$$\chi^2 = \sum_{i,j}(\sigma^i_{exp} - \sigma^i_{th})V^{-1}_{ij}(\sigma^j_{exp} - \sigma^j_{th}) \quad .$$

Here V is the error matrix, a sum of matrix A and matrix E:

$$V_{ij} = A_{ij} + \frac{\partial\sigma^i}{\partial E_i}\frac{\partial\sigma^j}{\partial E_j}E_{ij} \quad .$$

Matrix A accounts for the correlations between the cross sections, while matrix E accounts for the energy measurement errors. σ^i_{exp} is the measured cross section at the energy scan point i. σ^i_{th} is the theoretical cross section predicted by the model independent formula 1.2.

4.1.1 Error matrix for cross section measurements

As discussed in the previous chapter, the systematic uncertainties in the cross section measurements are mainly due to uncertainties in the event selection efficiency estimation and theoretical uncertainties in the luminosity determination.

The diagonal elements of error matrix A should contain the full statistical and systematic errors, calculated by:

$$A_{ii} = [(Lumi.Stat.Err.)^2 + (Lumi.Sys.Err.)^2$$

$$+(Eff.Sys.Err.)^2 + (Other.Sys.Err.)^2]\sigma_{ii}^2$$

where the *Lumi.Sys.Err.* and *Eff.Sys.Err.* are the luminosity systematic errors and efficiency systematic errors in the cross section measurements, and *Other.Sys.Err.* contains systematic errors from background subtraction. *Lumi.Stat.Err.* represents the statistical errors in the cross section measurements. As we discussed before, the cross section can be written as:

$$\sigma_{had} = \frac{N_{had}}{\mathcal{L}\epsilon} \quad .$$

Here N_{had} is the number of selected hadronic events after background subtraction and ϵ is the event selection efficiency. $\mathcal{L}$ is the measured luminosity which is determined by:

$$\mathcal{L} = \frac{N_{bhab}}{\sigma_{bhab}} \quad ,$$

where N_{bhab} is the number of the Bhabha events and σ_{bhab} is the calculated Bhabha cross sections within the acceptance of the SICAL. Using the above expressions, the statistical error for the cross section measurement can be shown to be:

$$(\Delta\sigma_{had})^2_{stat} = \frac{\sigma_{had}}{\mathcal{L}\epsilon} + \frac{\sigma^2_{had}}{N_{bhab}} \quad .$$

From the above formula, it is easy to see that the cross section statistical error depends on the measured luminosity. It should be pointed out that the cross section used in the above formula is taken from the model independent formula prediction rather than the measured value. This provides the best

estimate of the statistical errors and avoids biasing the fit due to downward measurement fluctuations.

For the off-diagonal elements of matrix A, we have to consider the correlations between systematic errors. For example, the fact that we have used the same Monte Carlo program BHLUMI [40] to estimate the Bhabha cross sections for the luminosity measurements made in each year's data means that the theoretical part of the systematic error is fully correlated among the data taken in different years. The experimental uncertainties on the luminosity measurement are only correlated if the detector is unchanged. This introduces year-to-year correlation due to the actual geometry of the detectors which is common to different years. Some errors are obtained from the data directly each year and thus are not correlated. Table 4.1 summarizes the luminosity systematic error correlations for the past five years [50].

Sys. err.	Year	1990	1991	1992 P	1992 S	1993
5.7E-3	1990	1.00	0.376	0.376	0.202	0.247
4.3E-3	1991	0.376	1.00	0.629	0.269	0.331
4.3E-3	1992 P	0.376	0.629	1.00	0.269	0.331
2.2E-3	1992 S	0.202	0.269	0.269	1.00	0.692
1.8E-3	1993	0.247	0.331	0.331	0.692	1.00

Table 4.1: Correlation matrix of the luminosity systematic errors for the past five years. The steady improvement in the relative luminosity systematic errors is due to improved understanding of the performance of the luminosity monitors. The drastic reduction of the systematic error for the second part of the 1992 data (1992 S) is the result of the installation of SICAL. The 1992 P denotes 1992 Pre-SICAL installation period.

For the hadronic event selection, we have used the same Monte Carlo generator to estimate the selection efficiencies for each year, so the efficiency systematic errors for different years' data are correlated. Considering all above correlations, we can write the off diagonal elements as [51]:

$$
\begin{aligned}
A_{ij} &= [(Lumi.Stat.Err.)^2 + (Lumi.Sys.Err.)^2]\sigma_i\sigma_j \\
&\quad \text{if measurements are at the same energy,} \\
&= [(Lumi.Sys.Err.)^2 + (Eff.Sys.Err.)^2]\sigma_i\sigma_j \\
&\quad \text{if measurements are in the same year,} \\
&= [(Eff.Sys.Err.)_i(Eff.Sys.Err.)_j(\rho_{ij}^{eff}) \\
&+ (Lumi.Sys.Err.)_i(Lumi.Sys.Err.)_j(\rho_{ij}^{lumi})]\sigma_i\sigma_j \\
&\quad \text{if measurements are in different years.}
\end{aligned}
$$

Here ρ_{ij}^{eff} is the correlation coefficient between the efficiency systematic errors in different years. ρ_{ij}^{lumi} is the correlation coefficient between the luminosity systematic errors for different years as listed in the Table 4.1.

4.1.2 Error matrix for LEP beam energy measurements

The energy uncertainty matrix E is constructed by considering the correlations between the systematic uncertainties in the energy measurements at each energy scan point. We classify the energy uncertainties into two categories, the correlated and uncorrelated ones. The correlated errors are

mainly due to the uncertainties in the absolute energy scale determined by the energy calibration. The uncorrelated errors include the relative point to point energy errors and the reproducibility of LEP machine settings (RF, dipole current). A detailed discussion of LEP beam energy errors is given in Appendix A.

So the diagonal elements of error matrix of energy measurements can be expressed as:

$$E_{ii} = [(Uncorr.Err)^2 + (Corr.Err)^2]E_i^2 \quad ,$$

where $Uncorr.Err$ and $Corr.Err$ represent relative uncorrelated and correlated errors in the energy scan points E_i. For the off diagonal elements of error matrix of energy measurement, only correlated errors are taken:

$$E_{ij} = (Corr.Err)^2 E_i E_j \quad .$$

For the data collected in 1993, LEP calibrated each of the three energy scan points using the resonant depolarization method. The errors in the absolute energy scale determination are reduced to about 1 MeV. Due to the frequent calibration of the off peak energy points, the total uncorrelated errors from point to point energy errors and energy reproducibility errors for the off peak points were reduced to about 2 MeV on the peak−2 energy point and 1.5 MeV for the peak+2 point. Since the peak energy scan point only had one calibration measurement, the reproducibility error for this point is

about 5.3 MeV. Table 4.2 [52] gives the error matrix for the 1993 energy scan.

	Peak−2	peak	Peak+2
Peak−2	4.96	1.98	1.97
peak	1.98	30.14	2.05
Peak+2	1.97	2.05	3.15

Table 4.2: Error matrix in MeV^2 for the 1993 energy scan.

4.2 The fit results

Two fits are performed to extract the Z resonance parameters. First, by using only the measured hadronic cross sections, Z lineshape parameters M_Z, Γ_Z, and σ^0_{had} are extracted. Then, by using the ALEPH measured leptonic cross sections, a combined fit is performed and parameters M_Z, Γ_Z,σ^0_{had}, and R_l are obtained.

4.2.1 Hadronic lineshape fit results

A three-parameter fit to the 1993 measured hadronic cross sections is performed using the model independent fitting package MIZA [21]. This fit yields the peak hadronic cross section σ^0_{had}, the Z mass and Γ_Z:

$$M_Z = 91.1921 \pm 0.0043\ GeV$$

$$\Gamma_Z = 2.4858 \pm 0.0073\ GeV$$

Parameter	Value	Stat. Error	Sys. Error LEP	Sys. Error Eff.	Sys. Error Lumi	Sys. Error 2γ
M_Z (MeV)	91192.1	3.8	1.7	-	0.8	-
Γ_Z (MeV)	2485.8	6.7	2.0	-	1.5	1.5
σ^0_{had} (nb)	41.636	0.080	0.016	0.029	0.074	0.014

Table 4.3: 1993 statistical and systematic errors on the measured Z resonance parameters.

$$\sigma^0_{had} = 41.636 \pm 0.115\ nb\ .$$

The χ^2 of the fit is 0.1 for 1 degree of freedom. Beside statistical errors, the uncertainties quoted in the above results include all sources of systematic errors. The uncertainty on M_Z due to the LEP energy uncertainties is about 1.7 MeV, and for Γ_Z it is 2.0 MeV[1]. A detailed discussion of the LEP energy errors on the Z mass and width is given in Appendix A. The other systematic errors are due to uncertainties in the hadronic cross section measurements, which include the luminosity systematic errors, the uncertainties in the hadronic event selection efficiency calculation, and the uncertainties in the two photon background estimation. Table 4.3 listed the contribution of the systematic errors from all sources. Figure 4.1 shows the hadronic cross sections measured from 1989 to 1993 together with the SM predictions.

[1]An additional error of 1 MeV due to an uncertainty of 5 MeV in the LEP center-of-mass energy spread has been added.

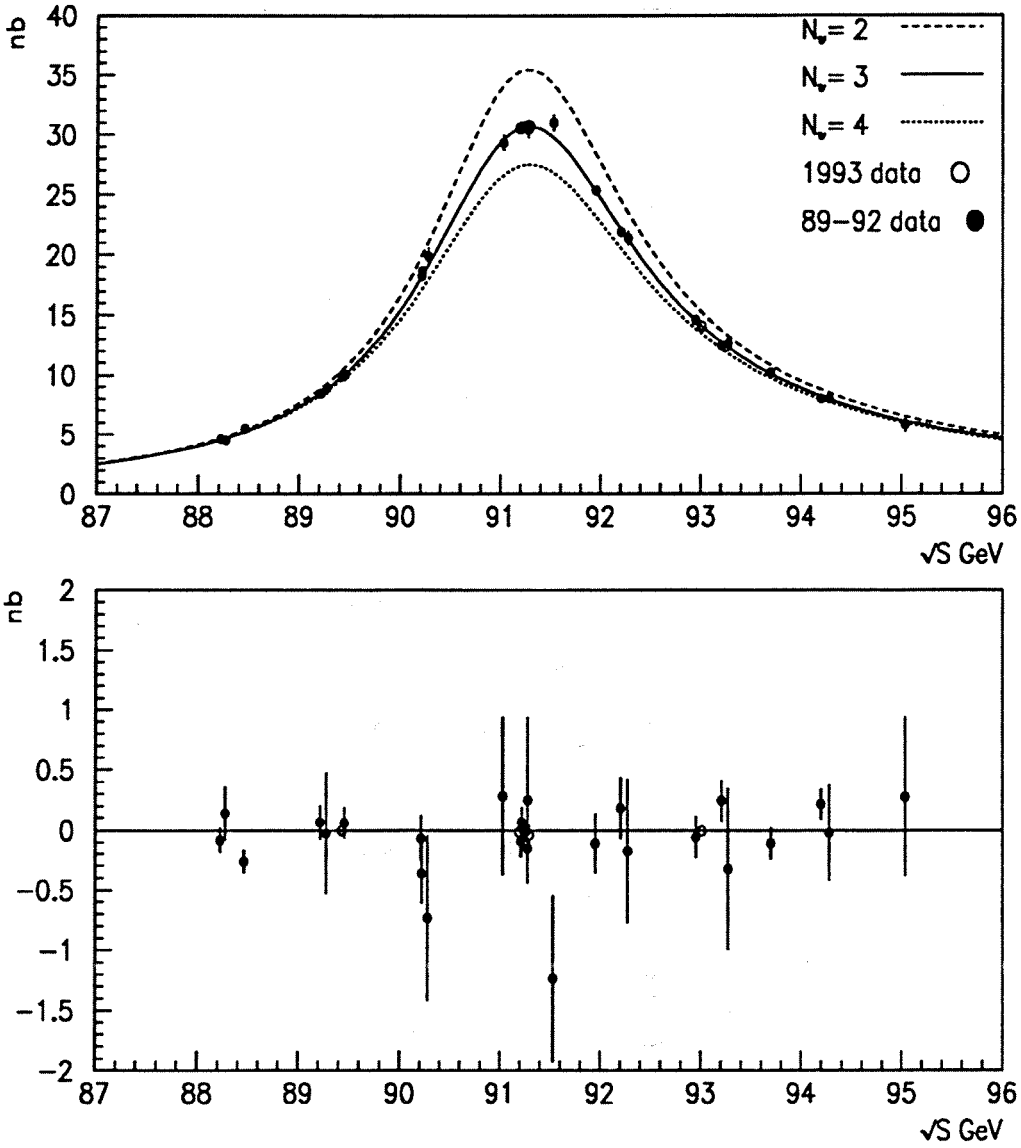

Figure 4.1: Cross sections for $e^+e^- \to$ hadrons as a function of center-of-mass energy. The SM predictions for $N_\nu = 2$, 3, and 4 are shown. The bottom plot shows the residuals of the fitted hadronic cross sections and the measured values.

4.2.2 Combined fit with leptonic lineshapes

Using ALEPH cross section measurements for the lepton channels ($e^+e^- \rightarrow Z \rightarrow l^+l^-,\ \ l = e, \mu, \tau$) [50], we can extract the peak leptonic cross sections $\sigma_l^0,\ \ (l = e, \mu, \tau)$ and the ratios:

$$R_e \equiv \Gamma_{had}/\Gamma_e,\ \ R_\mu \equiv \Gamma_{had}/\Gamma_\mu,\ \ R_\tau \equiv \Gamma_{had}/\Gamma_\tau\ .$$

For the combined lineshape fit of hadronic cross sections and leptonic cross sections, we fit for the following 6 parameters:

$$M_Z,\ \Gamma_Z,\ \sigma_{had}^0,\ R_e,\ R_\mu,\ R_\tau.$$

This set of parameters is chosen since these variables have little correlation with each other. Table 4.4 shows the parameters from the combined fit together with some derived results for the data taken from 1989 to 1993. The correlation matrix for these six parameters is shown in Table 4.5.

From Table 4.4, we can see that the measured ratios R_e, R_μ, and R_τ are consistent with each other, in agreement with lepton university. If we now assume exact lepton universality, which implies that $\Gamma_l = \Gamma_e = \Gamma_\mu = \Gamma_\tau$ (aside from very small mass effects), we can perform a 4-parameter fit ($M_Z,\ \Gamma_Z,\ \sigma_{had}^0,\ R_l$). The fit results together with some derived results are summarized in Table 4.6. The correlation matrix for these four parameters is shown in Table 4.7.

Parameter	1989-1993 Data
M_Z (GeV)	91.1914 ± 0.0039
Γ_Z (GeV)	2.4944 ± 0.0058
σ_{had} (nb)	41.63 ± 0.10
R_e	20.62 ± 0.13
R_μ	20.94 ± 0.12
R_τ	20.67 ± 0.12
$\chi^2/d.o.f.$	90/103
Γ_e (MeV)	84.32 ± 0.32
Γ_μ (MeV)	83.03 ± 0.55
Γ_τ (MeV)	84.09 ± 0.55
σ_e (nb)	2.018 ± 0.013
σ_μ (nb)	1.987 ± 0.012
σ_τ (nb)	2.013 ± 0.012

Table 4.4: Results of the combined fit with both hadronic and leptonic cross sections. The errors include both systematic and statistical uncertainties.

Parameter	M_Z	Γ_Z	σ_{had}	R_e	R_μ	R_τ
M_Z	1.000	0.043	0.022	0.031	0.002	0.006
Γ_Z	0.043	1.000	-0.320	-0.044	0.007	-0.019
σ_{had}	0.022	-0.320	1.000	0.149	0.153	0.161
R_e	0.031	-0.044	0.149	1.000	0.068	0.072
R_μ	0.002	0.007	0.153	0.068	1.000	0.075
R_τ	0.006	-0.019	0.161	0.072	0.075	1.000

Table 4.5: Correlation matrix for the set of parameters given in 4.4.

Parameter	1989-1993 Data
M_Z (GeV)	91.1916 ± 0.0039
Γ_Z (GeV)	2.4941 ± 0.0058
σ_{had} (nb)	41.63 ± 0.10
R_l	20.751 ± 0.074
$\chi^2/d.o.f.$	94/105
Γ_{had} (MeV)	1744.7 ± 5.3
Γ_l (MeV)	84.04 ± 0.23
σ_l (nb)	2.0052 ± 0.0077

Table 4.6: Results of the combined fit with both hadronic and leptonic cross sections assuming lepton universality. The errors include both systematic and statistical uncertainties.

Parameter	M_Z	Γ_Z	σ_{had}	R_l
M_Z	1.000	0.044	0.021	0.019
Γ_Z	0.044	1.000	-0.320	-0.036
σ_{had}	0.021	-0.320	1.000	0.249
R_l	0.019	-0.036	0.249	1.000

Table 4.7: Correlation matrix for the set the parameters given in Table 4.6.

Recall that Z total width can be expressed as:

$$\Gamma_Z = \Gamma_{had} + 3\Gamma_l + \Gamma_{inv},$$

where Γ_{inv} is the invisible width from Z decay into neutrinos. From the above results, we can derive $\Gamma_{inv} = 496.6 \pm 4.4$ MeV and $\Gamma_{inv}/\Gamma_l = 5.909 \pm 0.047$. By using the equation 1.3, we obtain the number of light neutrinos:

$$N_\nu = 2.966 \pm 0.024 \quad ,$$

which is consistent with the integer number 3.

As we discussed before, the parameter R_l can be used to determine the strong coupling constant α_s. Using equation 1.4 and the measured value $R_l = 20.751 \pm 0.074$, we obtain $\alpha_s(M_Z^2) = 0.119 \pm 0.012$, which is in good agreement with the independent value $\alpha_s(M_Z^2) = 0.123 \pm 0.006$ [15] extracted from jet event shapes measured in hadronic Z decays.

4.3 Interpretation of results

The precise electroweak measurement results obtained from the lineshape can be used to check the validity of the SM and, within its framework, to constrain some of its basic parameters which are not directly measured at LEP. In this section, we will first compare the measured Z lineshape parameters with the SM predictions. Then we will discuss the constraints on the top

quark mass set by the measured Z lineshape parameters together with the results from ALEPH lepton forward-backward asymmetry measurements, τ polarization measurements, results from quark asymmetries, and heavy flavor partial widths.

4.3.1 Comparison with the Standard Model

By taking the M_Z measured using the Z lineshape, $M_{top} = 176 \pm 13$ GeV [5], $\alpha_s(M_Z^2) = 0.123 \pm 0.006$ [15], $\alpha_{em}^{-1}(M_Z^2) = 128.896 \pm 0.090$ [19], and assuming $M_H = 300$ GeV, we can calculate the SM expected values for the lineshape parameters. Table 4.8 shows measured Z lineshape parameters compared with the SM predictions. From this table, we see that the measured lineshape

			errors		
Parameter	Measured Value	SM Value	ΔM_{top}	$\Delta\alpha_s$	$\Delta\alpha_{em}$
M_Z (GeV)	91.1916 ± 0.0039	input	–	–	–
Γ_Z(MeV)	2494.1 ± 5.8	2496.9 ± 4.6	3.2	3.2	0.6
Γ_l(MeV)	84.04 ± 0.23	83.96 ± 0.12	0.12	–	–
σ^0_{had}(pb)	41631 ± 103	41448 ± 33	8	32	1
$R_l \times 10^3$	20751 ± 74	20770 ± 40	4	40	4

Table 4.8: ALEPH measured Z lineshape parameters comparing with the SM predictions. The SM value errors only include the uncertainties from the input parameter M_{top}, $\alpha_s(M_Z^2)$, and $\alpha_{em}^{-1}(M_Z^2)$. Column three lists the contributions to the total errors from each of the input parameters. The SM errors are calculated using the ZFITTER 4.8 program [53].

parameters are in good agreement with the SM expected values. We can also

see that Γ_Z measurement gives the best constrain to the top quark mass, and R_l, Γ_Z, and σ^0_{had} measurements give good constraints to the strong coupling constant.

4.3.2 Constraint on the top mass

The observables measured at the Z resonance can be used to constrain the top quark mass in the context of the SM. In addition to the lineshape parameter Γ_Z, there are some other observables measured in ALEPH which are also sensitive to the top quark mass. They are the pole lepton forward-backward charge asymmetries $A^{0,l}_{FB}$ [50], and the τ polarization observables (the average polarization $\mathcal{P}_\tau$ and the forward-backward polarization asymmetry $A^{\mathcal{P}_\tau}_{FB}$) [54]. The observables measured with quarks [55] such as the charm and bottom quark forward-backward asymmetries $A^{b\bar{b}}_{FB}$ and $A^{c\bar{c}}_{FB}$, the Z partial widths Γ_b and Γ_c, and $sin^2\theta^{eff}_W$ from the hadronic charge asymmetry $\langle Q_{FB} \rangle$ measurements [56]. Most of these observables essentially gain their top quark mass dependence from the effective coupling constants, except for $\Gamma_{b\bar{b}}$, which also has a large contribution from the top quark mass dependent hadronic vertex corrections.

The pole asymmetries are related to the effective coupling constants $\hat{g}^f_V$ and $\hat{g}^f_A$ by:

$$A^{0,f}_{FB} \equiv \frac{3}{4}\mathcal{A}_e\mathcal{A}_f \ ,$$

where

$$\mathcal{A}_f \equiv \frac{2\hat{g}_V^f \hat{g}_A^f}{(\hat{g}_V^f)^2 + (\hat{g}_A^f)^2} \ .$$

The τ polarization observables are:

$$\begin{aligned} \mathcal{P}_\tau &= -\mathcal{A}_\tau \\ A_{FB}^{\mathcal{P}_\tau} &= -\frac{3}{4}\mathcal{A}_e \ . \end{aligned}$$

Table 4.9 summarizes the recent ALEPH measurements of these observables.

Parameter	Measured Value
$A_{FB}^{0,l}$	0.0208 ± 0.0026
A_τ	0.136 ± 0.015
A_e	0.129 ± 0.017
$R_b = \Gamma_{b\bar{b}}/\Gamma_{had}$	0.2206 ± 0.0031
$R_c = \Gamma_{c\bar{c}}/\Gamma_{had}$	0.165 ± 0.021
$A_{FB}^{0,b}$	0.094 ± 0.0068
$A_{FB}^{0,c}$	0.080 ± 0.023
$sin^2\theta_W^{eff}$ from $\langle Q_{FB} \rangle$	0.2317 ± 0.0017

Table 4.9: List of some top quark mass sensitive observables measured at ALEPH.

Figure 4.2 shows the measured Γ_Z compared with the SM predicted values as a function of the top quark mass M_{top}. Figure 4.3 and Figure 4.4 show the other ALEPH measured top sensitive observables together with their SM predictions as function of M_{top}. The bands in the SM predictions reflect the

linear sum of the expected variations of each quantity due to a change of the strong coupling constant $\alpha_s = 0.123 \pm 0.006$ and M_H in the interval $60 \leq M_H(GeV) \leq 1000$ for $M_Z = 91.1916$ GeV. The small Z mass uncertainty does not change the predictions.

A SM fit is performed using the measured lineshape parameters with the constraints listed in the Table 4.9, yielding a top quark mass and strong coupling constant as below:

$$M_{top} = 178^{+15}_{-16}\ ^{+16}_{-18}\ GeV$$

$$\alpha_s(M_Z^2) = 0.115 \pm 0.007 \pm 0.002 \quad ,$$

with $\chi^2/d.o.f. = 11/9$. The central values and the first set of errors refer to a Higgs mass $M_H = 300$ GeV. The second set of errors corresponds to the variation of the central value when M_H is varied in the interval $60 \leq M_H(GeV) \leq 1000$. The determined top quark mass is in excellent agreement with the recent direct measurements reported by CDF [5], $M_{top} = 176 \pm 8\ (stat.) \pm 10\ (sys.)$ GeV, and by D0 [6], $M_{top} = 199^{+19}_{-21}(stat.) \pm 22\ (sys.)$ GeV.

4.4 Summary

Hadronic cross sections are measured with the data collected in 1993. By fitting them with a model independent formula, the Z resonance parameters M_Z, Γ_Z, and σ^0_{had} are obtained. A combined fit with both hadronic and

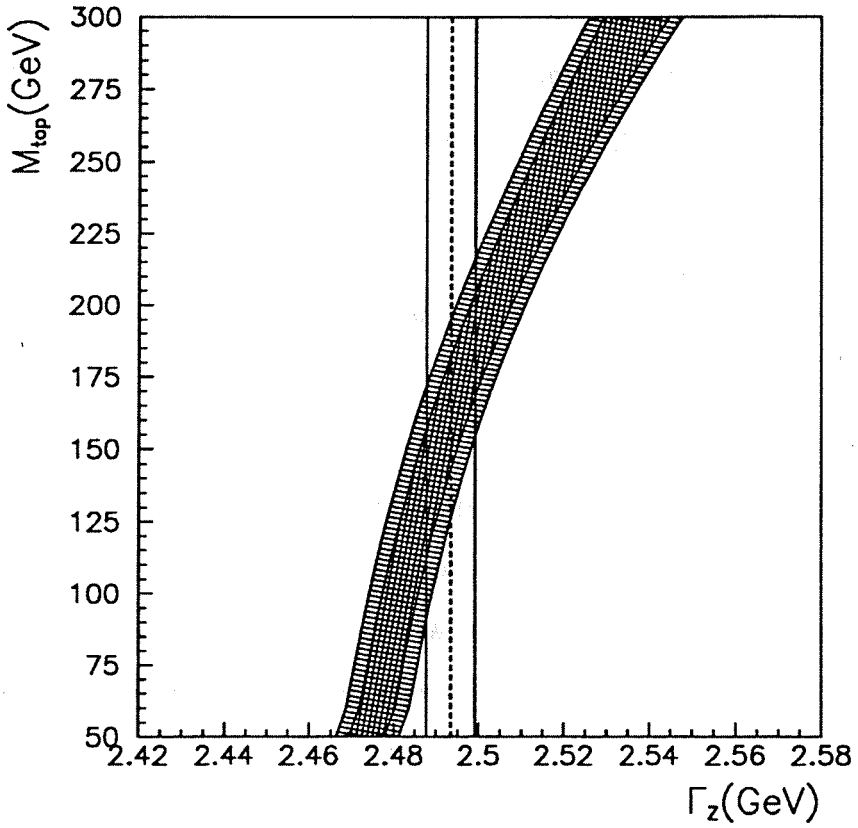

Figure 4.2: Comparison of the Γ_Z with the SM prediction as a function of top mass M_{top}. The cross hatched area shows the variation of the SM prediction with M_H spanning the interval $60 \leq M_H(GeV) \leq 1000$ and singly-hatched area corresponds to a variation of α_s within the interval $\alpha_s = 0.123 \pm 0.006$. The total width of the band corresponds to the linear sum of both uncertainties. The experimental errors on the parameters are indicated as vertical lines.

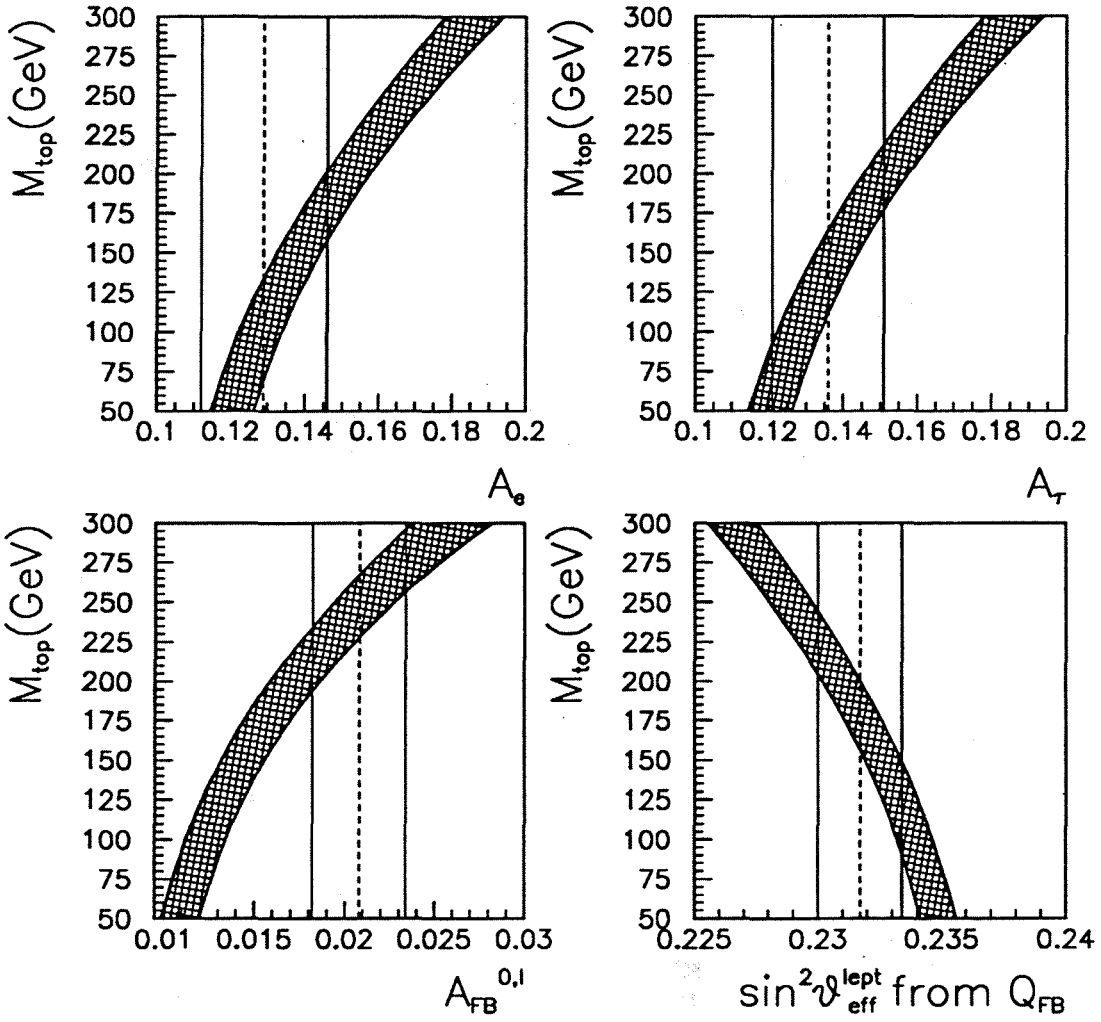

Figure 4.3: Comparison of the measured ALEPH top quark mass sensitive observables with the SM predictions as a function of top mass M_{top}. The cross hatched area shows the variation of the SM prediction with M_H spanning the interval $60 \leq M_H(GeV) \leq 1000$. The experimental errors on the parameters are indicated as vertical lines.

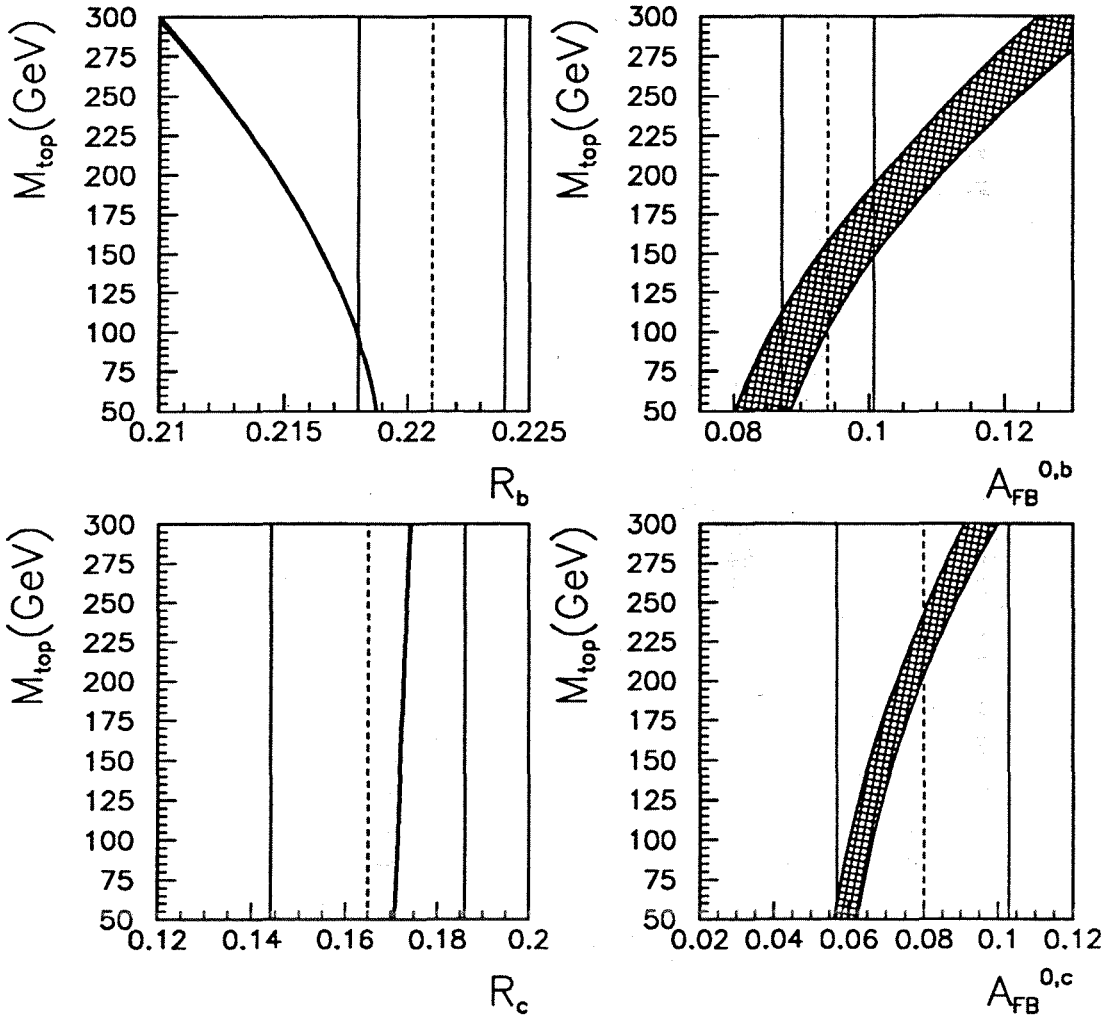

Figure 4.4: Comparison of the measured ALEPH top sensitive observables with the SM predictions as a function of top mass M_{top} (*c.f.* figure 4.3).

leptonic cross sections measured with the data taken from 1989 to 1993 yields:

$$\begin{aligned} M_Z &= 91.1916 \pm 0.0039\ GeV \\ \Gamma_Z &= 2.4941 \pm 0.0058\ GeV \\ \sigma^0_{had} &= 41.63 \pm 0.10\ nb\ . \end{aligned}$$

The partial widths of Z decays $(\Gamma_e, \Gamma_\mu, \Gamma_\tau)$ and ratios of hadronic partial width to leptonic partial widths (R_e, R_μ, R_τ) are also determined from the combined fit. The measured ratios are:

$$\begin{aligned} R_e &= 20.62 \pm 0.13 \\ R_\mu &= 20.94 \pm 0.12 \\ R_\tau &= 20.67 \pm 0.12\ . \end{aligned}$$

The measured ratios from each lepton channel showed consistency with lepton university. By assuming lepton universality, the following electroweak parameters are obtained:

$$\begin{aligned} \Gamma_{had} &= 1744.7 \pm 5.3\ MeV \\ \Gamma_l &= 84.04 \pm 0.23\ MeV \\ \Gamma_{inv} &= 496.6 \pm 4.4\ MeV \\ R_l &= 20.751 \pm 0.074 \\ \Gamma_{inv}/\Gamma_l &= 5.909 \pm 0.047\ . \end{aligned}$$

The above measured lineshape parameters are in good agreement with the SM expected values. Using the SM value of the ratio of neutrino partial width to lepton partial width $\Gamma_\nu/\Gamma_l = 1.992 \pm 0.003$, the number of light neutrinos species $N_\nu = 2.966 \pm 0.024$ is determined by the Γ_{inv}/Γ_l measurement.

By combining the Z lineshape measurements with other electroweak observables measured at ALEPH, we are able to constrain the top quark mass and the strong coupling constants in the context of the SM. From a SM fit, we get:

$$M_{top} = 178^{+15\ +16}_{-16\ -18}\ GeV$$

$$\alpha_s(M_Z^2) = 0.115 \pm 0.007 \pm 0.002 \quad .$$

The central values and the first set of errors refer to a Higgs mass $M_H = 300$ GeV. The second set of errors corresponds to the variation of the central value when M_H is varied in the interval $60 \leq M_H(GeV) \leq 1000$. The top quark mass obtained here is consistent with the direct measurements reported by CDF [5], $M_{top} = 176 \pm 8\ (stat.) \pm 10(sys.)$ GeV, and by D0 [6], $M_{top} = 199^{+19}_{-21}(stat.) \pm 22\ (sys.)$ GeV.

Appendix A

LEP Energy Calibration

A.1 Energy calibration by resonant depolarization

At LEP, beam particles are naturally spin polarized along the vertical direction of the bending field due to a small asymmetry in synchrotron radiation [29]. The degree of beam polarization can be measured by using a Compton scattering polarimeter [57], based on the idea that the angular distribution of the back-scattered circularly polarized photons from transversely polarized beam particles depends on both the polarization of photons and on that of the beam particles.

The polarization build-up is a very slow process in the LEP storage ring; the calculated rise time is about 310 minutes at 46 GeV beam energy and a maximum polarization of 92.4% can theoretically be achieved. Under real

operating conditions, due to imperfections in the beam optics, such as vertical orbit distortions and dispersions, uncompensated solenoids, beam-beam effect, etc., the amount of polarization is very small ($< 10^{-2}$). A special procedure has been commissioned which compensates for some of these imperfections in order to increase the level of beam polarization. The first observation of transverse polarization in LEP was achieved in 1990 [28], and typical polarizations of 10-20% are measured during the energy calibration. From a dedicated experiment a maximum transverse polarization of 57% has been observed [58].

The polarized beam particles, electrons or positrons spin precess about the LEP dipole field. The spin precession frequency is related to the beam revolution frequency as:

$$f_{spin} = \nu_s f_{rev}$$

where at LEP $f_{rev} = 11245.5041(1)$ Hz. ν_s is the number of precessions per turn (spin tune), which is related to the beam energy E_{beam} by:

$$\nu_s = a_e \gamma = \frac{(g_e - 2)}{2} \frac{E_{beam}}{m_e c^2} = \frac{E_{beam}}{0.4406486(1)} \ .$$

Here $a_e = \frac{1}{2}(g_e - 2) = 1.1596521884(43) \times 10^{-3}$ is the electron anomalous magnetic moment and $m_e c^2 = 0.51099906(15)$ MeV is the electron mass. It is clear that if one can measure the spin tune ν_s or the spin precession frequency f_{spin} to a high precision, one can accurately determine the beam energy E_{beam}.

The spin precession frequency of the polarized beam particles is precisely measured by inducing a resonant depolarization with a horizontal oscillating magnet. The measurement is done by putting a weak horizontal oscillating magnetic field at one point of the LEP ring and slowly sweeping the frequency of the oscillating magnet until it is in phase with the beam particle spin precession. At this point the spin rotations about the horizontal direction will add coherently and depolarize the beam. Since the beam encounters the horizontal exciting field only once per turn, the frequency of the resonant depolarization f_{dep} actually depends on the fractional part of the spin tune $[\nu_s]$ and also on its mirror fraction $1-[\nu_s]$:

$$f_{dep} \equiv f_{spin} = [\nu_s] f_{rev}$$

or

$$f_{dep} \equiv f_{spin} = (1-[\nu_s]) f_{rev}$$

The beam energy E_{beam} can be determined by:

$$E_{beam} = \frac{m_e c^2}{a_e} = (N_s + \frac{f_{dep}}{f_{rev}}) 0.44064861(1) GeV$$

where the integer part of the spin tune N_s is known from the settings of LEP bending fields (N_s =105 at 45.6 GeV beam energy). The mirror ambiguity of fraction of the spin tune can be resolved easily by a small change of the beam energy.

Experimentally, the frequency of the oscillating magnet field is slowly

varied with time over a given range. In a simple approach, defining $\Delta\nu_{scan}$ as the difference in frequency between the start and the end of the sweep, the change in the beam particle polarization $P_{final}/P_{initial}$ in the resonant depolarization process can be described using the formula [59]:

$$\frac{P_{final}}{P_{initial}} = 2e^{-\chi} - 1 \ ,$$

where

$$\chi = \frac{(\pi\nu_s b_x l/BL)^2 f_{rev}}{\Delta\nu_{scan}/\Delta t} \ .$$

Here $b_x l \simeq 2 \times 10^{-4} Tm$ is the oscillating magnetic field and BL is the integrated guide field of LEP. The weak oscillating field $b_x l$ kicks the beam particle's spin about $140\mu rad$ down towards the horizontal plane with each turn, thus it needs about 10^4 turns (about 1 second) to rotate the spin vector completely down to the horizontal plane. Figure A.1 schematically shows the process of a beam particle's resonant depolarization at LEP. The perturbation from the oscillating magnet can be considered as an artificial spin resonance which is excited at some known location in spin tune. If the average spin tune of the beam is inside the width of the spin resonance, then the polarization vector is rotated. In the absence of beam energy spread, the magnitude of the polarization vector would not change and a value of $P_{final}/P_{initial} = -1$ could be obtained. However, because of the beam energy spread, the horizontal component of the polarization is quickly reduced, and the polarization can only be partially flipped. An example of energy

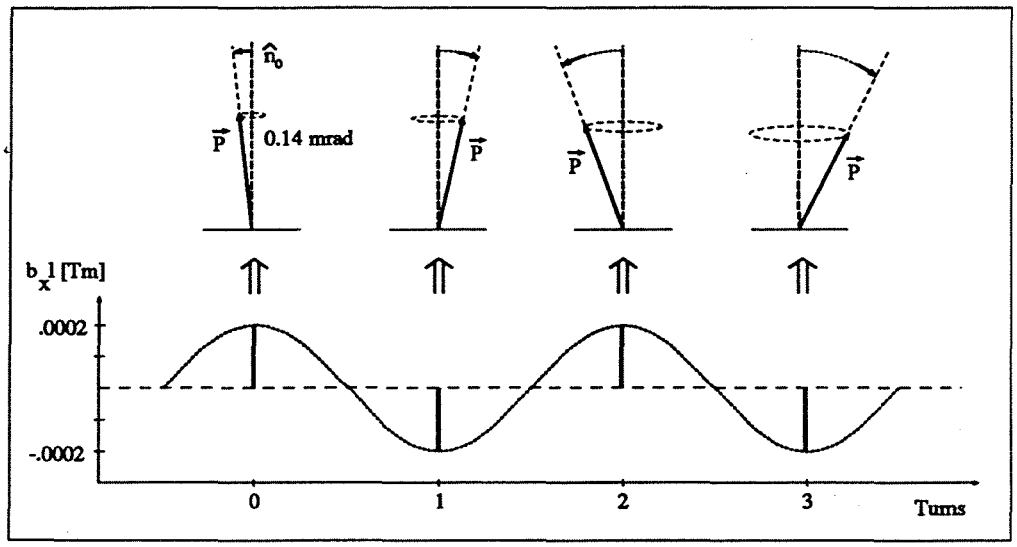

Figure A.1: Resonance condition between the nominal spin precession with $[\nu_s] = 0.5$ and the horizontal perturbation $b_x l$ from the LEP oscillating magnet. In an ideal storage ring , the polarization vector is initially along the vertical direction. After being tilted, the spin vector $\vec{P}$ precesses with frequency ν_s about its initial direction. If the perturbation is in phase with the nominal spin precession (in this example $f_{dep} = 0.5 f_{rev}$), the polarization vector is resonantly rotated away from the vertical direction.

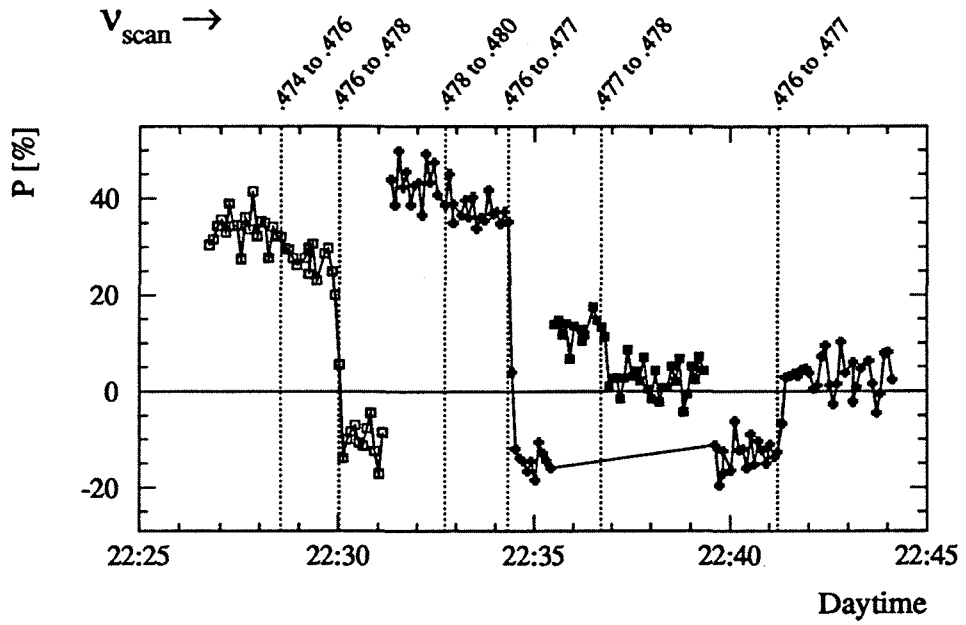

Figure A.2: Example of energy calibration. Several bunches are used to measure the non-integer part of the spin tune. Spin flip to negative polarization was observed and checked by flipping it again.

calibration by resonant depolarization is shown in Figure A.2.

Due to the fact that the polarization vector is an ensemble average over all the beam particle spin vectors and that the depolarization process occurs slowly compared to the periods of the betatron and synchrotron oscillations of the beam particles, the measured beam energy is to very good approximation independent of betatron and synchrotron oscillations of the individual particles and its accuracy is not limited by the beam energy spread (38 MeV). This fact also can be verified by measuring the FWHM of the spin depolarization resonance, which is as small as 0.2 MeV for a standard LEP energy

calibration settings (see Figure A.3.)

As discussed above, the spin tune measurement uncertainty determines the accuracy of the beam energy measurement. The resolution of the spin tune depends on the frequency difference $\Delta\nu_{scan}$ of the oscillating magnet during the sweep of the resonant depolarization process. So one can write the following relations:

$$\Delta\nu_{scan} = \Delta\nu_s = \Delta(f_{dep})/f_{rev} \quad ,$$

and the RMS uncertainty of the beam energy can be expressed as:

$$(\frac{\Delta E}{E})_{beam} \equiv \frac{1}{\sqrt{12}}\frac{\Delta\nu_s}{\nu_s} \quad .$$

For standard energy calibration, $\Delta\nu_{scan}$ is set to 0.002, giving an accuracy on the beam energy of $\Delta E = \pm 0.25$ MeV.

A.2 Corrections to LEP beam energy measurements

The beam energy of LEP is subject to fluctuations due to LEP settings (RF frequency, dipole current, etc.) and the various changes of environmental conditions such as magnet temperature, and beam orbit changes due to geological and tidal effects.

The circulating electron and positron beams move on a central orbit

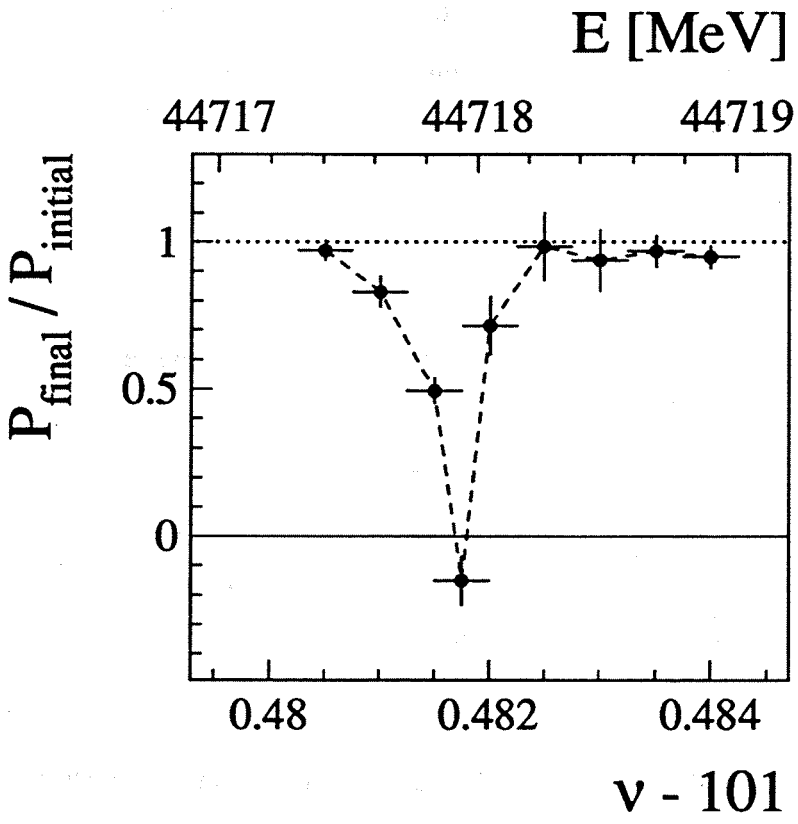

Figure A.3: A measurement of the artificially excited spin resonance. The slightly asymmetric resonance shape is due to tidal changes of the beam energy during the 12 minutes of measurement.

which length is defined by the RF frequency, which is nominally set to 352 254 170 Hz and measured to be better than 1 Hz. Particles moving out of the orbit will see different RF accelerating fields and will put them back on the central orbit.

There are two kinds of magnetic fields which affect the beam energy: dipole fields and quadruple fields. Dipole fields represent the bending magnetic fields around the ring. Since beams are constrained to move on the orbit defined by the RF frequency, the higher the $\int Bdl$ seen by the beam particles, the higher their energy should be. At LEP, the dipole current is the major cause for the changes of dipole fields. Since the LEP bending magnets are made of iron and concrete, the magnet temperature is another factor for the changes of dipole fields.

The quadruple fields are used to focus the beam particles. The beam particles will see an extra magnetic field if the average beam position is not in the center of the quadruple magnets. Since the beam orbit is fixed by the constant RF frequency, any changes in the LEP circumference will force the beam particles to move off center in the quadruples where they will receive extra deflection and thus lead to change the beam energy. In practice, the LEP ring is influenced by terrestrial tides [61] (see Figure A.4) and other local long term geological ground movements. The energy of LEP changes by about 1 MeV for a 13 μm transverse movement of the beam relative to the center of the quadrupoles [62]. Figure A.5 shows the transverse beam position in 1993 and its effect on the beam energy.

The circulating electrons and positions lose about 125 MeV per turn in

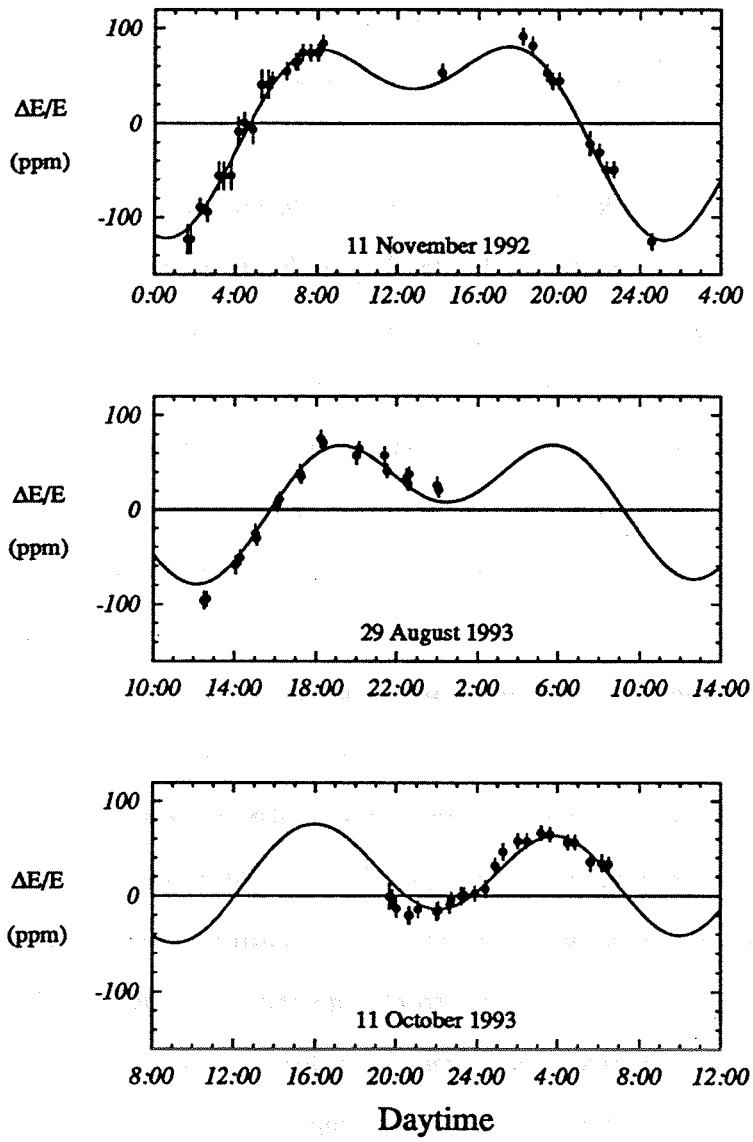

Figure A.4: Results of dedicated tide experiments. The beam energy measured with resonant depolarization has been corrected for changes of the integrated dipole field. The agreement between model and measurements is good.

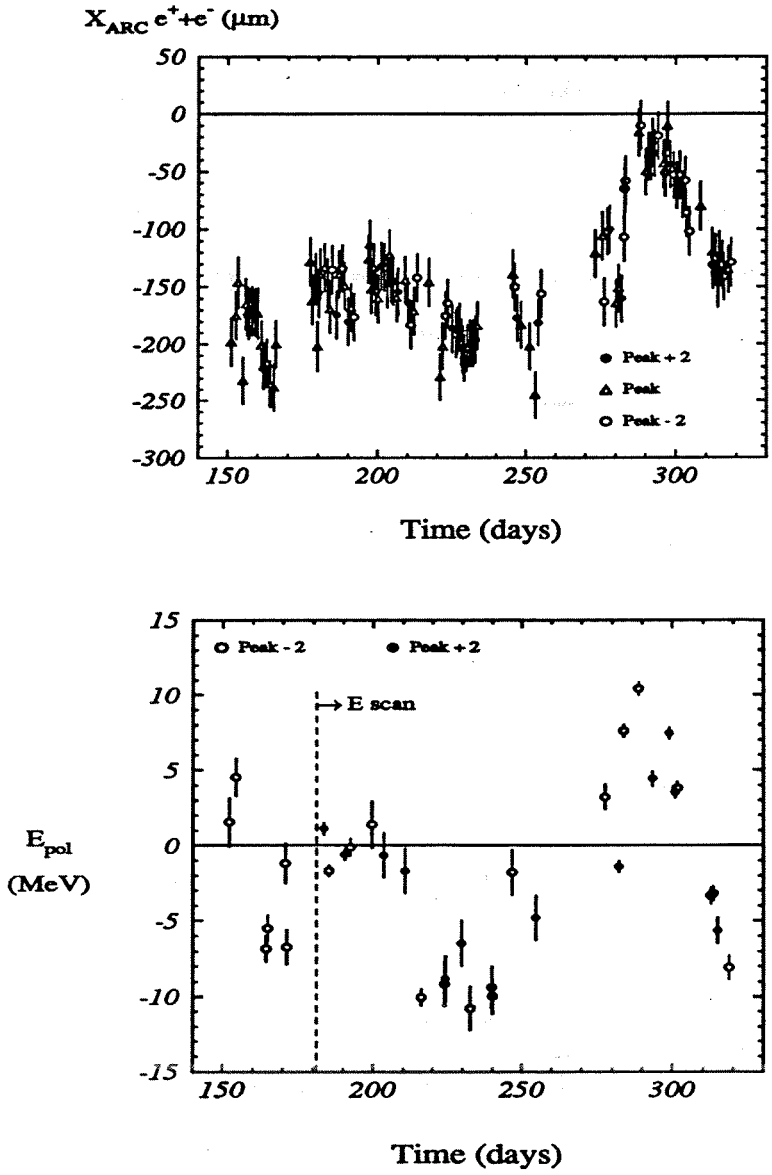

Figure A.5: Top: Mean X position of the beam versus time in 1993. Bottom: Average beam energy measured by resonant depolarization versus time in 1993. The energy has been corrected for changes in the integrated dipole field and tidal effects. A beam energy change due to the local long term geological ground movements is observed.

synchrotron radiation on their curved path through the LEP dipoles. This energy loss is compensated by acceleration in the radio frequency (RF) cavities, placed on both side of the LEP interaction point 2 and 6 . Ideally, the sum of the e^+ and e^- energies would be constant around the whole ring. Due to alignment errors, this is not necessarily the case, and corrections to the center of mass energy at the collision regions, especially those close to the RF sections (point 2 and point 6) have to be considered.

The influence of all above factors on the LEP energy results in typical changes in the center-of-mass energy of the order of 1 MeV per hour. So the accurate corrections to the LEP beam energy rely on frequent login of the LEP machine conditions, since the beam energy calibration by resonant depolarization only infrequently measures the instantaneous energy of the beam. To calculate the energy of LEP at some specific time t and fill, a model has been built as shown below:

$$\begin{aligned} E_{LEP} = \; & C_{norm}(fill) \\ & \times (Dipole\ field\ correction)(t) \\ & \times (Magnet\ temperature\ correction)(t) \\ & \times (Tidal\ correction)(t) \\ & \times (Orbit\ correction)(fill) \\ & \times (RF\ correction)(fill) \ . \end{aligned}$$

C_{norm} is the normalization factor determined by energy calibration using resonant depolarization method. If the fill is calibrated, then C_{norm} ensures

the energy of the model at the moment of the calibration equals the value of the calibration of this fill; if the fill is not a calibrated one, then C_{norm} takes the mean of all the calibrated fills at that energy scan points. The dipole field is constantly monitored by using a NMR probe installed inside a reference magnet which is connected in series with the LEP main bending magnets. The magnet temperature is monitored by 34 sensors uniformly distributed around the LEP tunnel. The tidal effect is corrected by using a geological model [63]. The orbit correction, applied once per fill, takes care of the long term local ground movement.

A.3 The uncertainties of LEP beam energy determination

The uncertainty in the LEP beam energy is mainly from three sources: the LEP energy reproducibility error on a fill to fill basis, the LEP energy uncertainty within a fill; and the uncertainty due to any further assumptions made. The reproducibility error is estimated from the scatter of the difference between the LEP energy predicted from the model with a constant normalization factor and the LEP beam energy measured by using the resonant depolarization method. Figure A.6 shows the scatter for all calibrated fills of 1993 off peak scan.

From the plot, a scatter of RMS 2.9 MeV and 7.0 MeV in the LEP center-of-mass energies of peak+2 and peak−2 are observed respectively. Provided

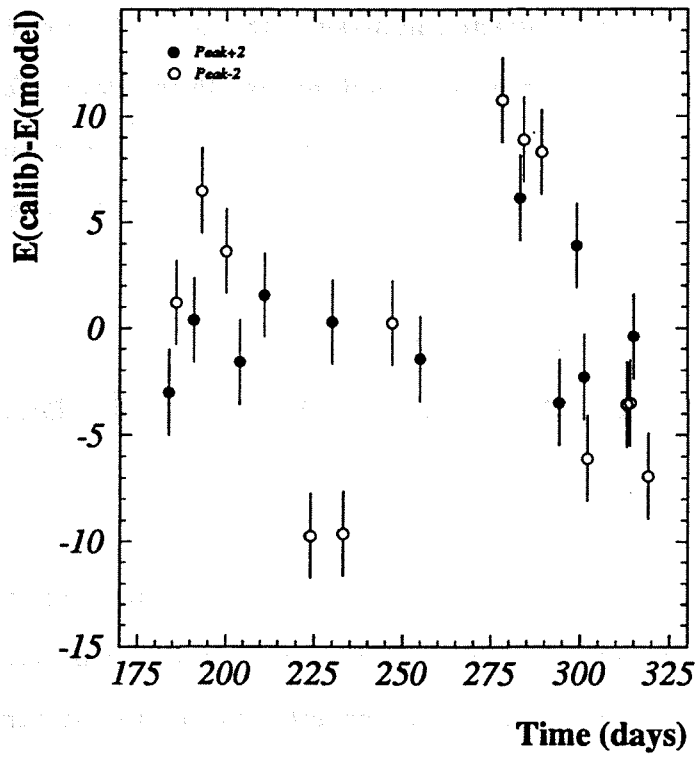

Figure A.6: Difference between the center-of-mass energies measured by the resonant depolarization method and those predicted by the model with a constant normalization factor. An error bar of 2 MeV is shown on each entry.

that calibrated fills are an unbiased sample of all fills, an error on the LEP beam energy due to the reproducibility of LEP for uncalibrated fills can be estimated by $\frac{\sigma_{cal}}{\sqrt{N_{uncal}}}$, where σ_{cal} is the RMS of the scatter and N_{uncal} is the number of uncalibrated fills. For 1993 scan, this gives center-of-mass error 0.6 MeV for peak+2 and 1.4 MeV for peak−2 energy points. This error is uncorrelated between energy points. For calibrated fills this error does not apply.

For the LEP energy uncertainty during the fill, for the uncalibrated fills the major uncertainty is from the normalization factor C_{norm} estimation. Since we have used a finite number of calibrated fills to estimate the mean energy, the error of this estimation is given by $\frac{\sigma_{cal}}{\sqrt{N_{cal}}}$. This yields an error in center-of-mass energy of 0.9 MeV for peak+2 and 1.9 MeV for peak−2 energy points. This error is also uncorrelated between energy points.

The total error due to C_{norm} and the reproducibility error of LEP for all fills, is determined by:

$$\frac{N_{uncal}}{N_{tot}}\left(\frac{\sigma_{cal}}{\sqrt{N_{cal}}} \oplus \frac{\sigma_{cal}}{\sqrt{N_{uncal}}}\right) = \frac{\sigma_{cal}\sqrt{N_{uncal}}}{\sqrt{N_{total}}\sqrt{N_{cal}}} .$$

This implies errors of 0.7 and 1.6 MeV in center-of-mass energy for the peak+2 and peak−2 points respectively.

There is an assumption made in the model of LEP energy calculation, it assumes that during a fill, the dipole field current measured in the reference magnet should reflect the main ring dipole current. It has been found that the measured dipole current from the NMR showed occasional jumps and

drifts during the fill, which could not be attributed to the changes in current or temperature. It is believed that at least part of these drifts and jumps is an artificial effect of the monitoring system in the reference magnet. To estimate this uncertainty, a conservative systematic error of 0.8 MeV in center-of-mass energy has been assigned to the peak+2 and peak−2 scan points. This error is correlated between the scan points.

Another assumption made in the LEP energy determination is that positron beam energy is equal to the electron beam energy. At LEP the energy calibration was performed only with electron beams. A dedicated resonant depolarization energy calibration test on the positron beams showed that the positron beam energy is the same as electron beam within the error of 0.2 MeV.

There are also uncertainties from the various corrections in the LEP energy determination. The largest error is from RF corrections, which contribute about 1 MeV for both peak−2 and peak+2 scan points. This error is almost fully correlated between energy points. The other corrections (tide, orbit, and temperature) contribute about 0.3 MeV uncorrelated errors and about 0.7 MeV correlated error for both off peak points. A detailed discussion of the errors due to the various corrections can be found in reference [52]. Table A.1 lists the systematic errors on the off-peak energies.

Source	Peak−2	Peak+2	Correlation	Corr. Error	Uncorr. Error
Mean fill energy	1.60	0.72	0	NA	NA
Dipole field uncertainty	0.93	0.93	0.81	0.8	0.4
Polarization systematics	0.50	0.50	0.04	0.1	0.5
e^+ Energy Uncertainty	0.30	0.30	0.5	0.2	0.2
RF Corrections (ALEPH)	1.02	1.02	0.96	1.0	0.1
Tide/orbit/temp	NA	NA	NA	0.7	0.3

Table A.1: Summary of errors (MeV) on the energy determination. These numbers are for illustration only - the exact errors are determined using the correlation matrix formalism. The first three columns give the errors at peak−2 and peak+2 and their correlation coefficient. The last two columns give the correlated and uncorrelated error as explained in the text. NA= Not Applicable.

A.4 LEP energy errors on M_Z and Γ_Z

For an energy scan at peak−2 and peak+2 points across the Z resonance, to a very good approximation, the systematic errors on M_Z due to the LEP energy uncertainty can be expressed as:

$$\Delta M_Z \approx 0.5\Delta(E_{-2} + E_{+2}) \ .$$

Here E_{-2} and E_{+2} are the luminosity-weighted center-of-mass energies at the two off-peak points. The systematic errors for Γ_Z due to the LEP energy uncertainties can be estimated by:

$$\frac{\Delta\Gamma_Z}{\Gamma_Z} \approx \frac{\Delta(E_{+2} - E_{-2})}{E_{+2} - E_{-2}} \ .$$

From the above formulae, it is easy to see that M_Z is sensitive to the full errors on the off peak energies, while Γ_Z is only sensitive to the uncorrelated energy systematic errors. Table A.2 summarizes various contributions of the LEP energy errors to the uncertainty of M_Z and Γ_Z.

Source	$\Delta\Gamma_Z(MeV)$	ΔM_Z (MeV)
Calibration scatter	1.3	0.9
Dipole field uncertainty	0.4	0.9
Polarization systematics	0.5	0.4
Tide/Orbit/Temp corrections	0.3	0.5
e^+/e^- energy difference	0.2	0.2
RF correction(ALEPH)	0.1	0.7
Total	1.5	1.6

Table A.2: Summary of sources of LEP energy errors on the M_Z and Γ_Z. These numbers are for illustration only, the exact errors have to be determined using the energy correlation matrix.

From the table, the total LEP energy error on the Z width is 1.5 MeV, and the LEP energy error on the Z mass is 1.6 MeV. The dominant LEP energy error on the Z width is from scatter of the energy calibration. For the Z mass, the dominant LEP errors are from both scatter of the energy calibration and uncertainty of the dipole field. In the lineshape fit, the exact errors have to be evaluated using correlation matrix formalism, which gives the LEP energy errors on the Z width of 2.0 MeV and Z mass of 1.7 MeV. .

Bibliography

[1] S. L. Glashow, Nuc. Phys. **B22** (1961) 579;
S. Weinberg, Phys. Rev. Lett. 19 (1967) 1264;
A.Salam, in Proc. of the 8th Nobel Symp., p.367, ed. N. Svartholm, Almqvist, and Wiksell, Stockholm, 1968.

[2] I. Hinchliffe, *Review of Particle Properties*, Phys. Rev. **D 50** (1994) 1297.

[3] P. Langacker and J. Erler, *Review of Particle Properties*, Phys. Rev. **D 50** (1994) 1304.

[4] Particle Data Group, *Review of Particle Properties*, Phys. Rev. **D 50** (1994).

[5] F.Abe *et al.*, CDF Collab., FERMILAB-PUB-95/022-E (Feb. 1995).

[6] S.Abachi *et al.*, D0 Collab., FERMILAB-PUB-95/028-E (Feb.1995).

[7] Chris Quigg, *"Gauge Theories of the Strong, Weak, and Electromagnetic Interactions"*, Benjamin/Cummings Publishing Company, 1983.

[8] P. W. Higgs, Phys. Lett. **12** (1964) 132 and Phys. Rev. Lett. **13** (1964) 508 and Phys. Rev. **145** (1966) 1156;
F. Englert and R. Brout, Phys. Rev. Lett. **13** (1964) 321.

[9] Francis Halzen and Alan D. Martin, *"Quarks and Leptons"*, John Wiley & Sons, 1984.

[10] A.s. Goldhaber *et al.*, Phys. Rev. **109** (1958) 1015.

[11] The LEP Collaborations ALEPH,DELPH,L3,OPAL and The LEP Electroweak Working Group, *A Combination of Preliminary LEP Electroweak Results for the 1995 Winter Conferences*, LEPEWWG/95-01, ALEPH 95-038 PHYSIC 95-036 (17 March 1995).

[12] Vernon D. Barger and Roger J. N. Philips, *"Collider Physics"*, Addison Wesley, 1987.

[13] F.A.Berends, *'Z Physics at LEP I'*, CERN 89-08, eds. G. Altarelli, *et al.*, vol. 1, (1989) 89.

[14] S.G.Gorishny, A.L.Kateyev and S.A.Larin, Phys. Lett. **B259** (1991) 144; L.R. Surguladze and M.A. Samuel, Phys. Rev. Lett. **66**(1991) 560.

[15] S.Betheke, Proceedings of the Linear Collider Workshop in Waikoloa, Hawaii, April 1993.

[16] F.Abe et al., CDF Collab., Phys. Rev. Lett. **73** (1994) 225.

[17] M. L. Swartz, *Reevaluation of the Hadronic Contribution to* $\alpha(M_Z^2)$, SLAC-PUB-6710, November 1994.

[18] A. D. Martin and D. Zeppenfeld, *A determination of the QED Coupling at the Z pole*, MAD/PH/855,DTP/94/110, November 1994.

[19] S. Eidelmann and F. Jegerlehner, *Hadronic contributions to* $(g-2)$ *of the leptons and to the effective fine structure constants* $\alpha(M_Z^2)$, PSI-PR-95-1, BUDKERINP 95-5, January 1995.

[20] M. Consoli *et al.*, *'Z Physics at LEP I'*, CERN 89-08, eds. G. Altarelli, *et al.*, vol. 1, (1989) 7.

[21] M. Martinez *et al.*, *Model Independent Fit to the Z Lineshape*, Z. Phys. **C49** (1991) 645.

[22] F.A. Berends *et al.*, Phys. Lett. **B203** (1988) 177.

[23] T.Hebbeker *et al.*, Phys. Lett. **B331** (1994) 165.

[24] M. Martinez and F. Teubert, IFAE-UAB 94-01.

[25] "LEP Design Report," Preprint CERN-LEP/84-01, CERN, 1984; *Large Electron-Positron Storage Ring, Technical Notebook*, (CERN Publication, November 1989).

[26] J. Billan, J.P.Gourber, K.N. Henrichsen and L.W. Walckiers, *Field Display System for the Forecast of Beam Momentum and Betatron Frequen-*

cies at LEP, XIV Int. Conf. on High Energy Accel., Tsukuba, Japan (August 1989) and Part. Accel. 29 (1990) 215.

[27] R.Baily *et al.*, *LEP Energy Calibration*, 2nd European Particle Accelerator Conference, Nice, France (June 1990) and CERN SL/90-95 (1990).

[28] L.Knudsen *et al.*, Phys. Lett. **B270** (1991) 97-104.

[29] A.A.Sokolov and I.M.Ternov, Sov. Phys. Dokl. **8** (1964) 1203.

[30] D. Decamp *et al.*, ALEPH Collab., Nucl. Inst. Meth. **A294** (1990) 121.

[31] D. Buskulic *et al.*, ALEPH Collab., *Performance of the ALEPH Detector at LEP*, CERN-PPE/94-170 (1994).

[32] G. Batignani *et al.*, 1991 IEEE Nuclear Science Symposium, Santa Fe, IEEE transactions on nuclear science, V.NS 39(4-5) (1992) Vol. 1 p.438.

[33] G.J.Barber *et al.*, Nucl. Instr. Meth. **A279** (1989) 212.

[34] W.B. Atwood *et al.*, Nucl. Instr. Meth. **A306** (1991) 446.

[35] Ralph Assmann, Robert Johnson and Zhong Feng, *Calibration of the ALEPH dE/dx*, ALEPH 94-116.

[36] D. Bederede *et al.*, *SICAL - a high precision silicon-tungsten luminosity calorimeter for ALEPH*, CERN-PPE/95-017, (Feb. 1995).

[37] J. A. Wear, *Measurement of the Number of Light Neutrino Generations, Z Resonance Parameters, and Absolute Luminosity at the ALEPH Detector*, Ph.D. thesis, University of Wisconsin-Madison, 1991.

[38] D.Decamp *et al.*, ALEPH Collab., Z. Phys. C. - Particles and Fields, **48** (1990) 365-391.

[39] F.A. Berends and R. Kleiss, Nucl. Phys. **B186** (1981) 22.

[40] S. Jadach, E. Richter-Wąs, Z. Wąs and B.F.L. Ward, Phys. Lett. **B268** (1991) 253;
S. Jadach, E. Richter-Wąs, Z. Wąs and B.F.L. Ward, Comput. Phys. Commun. **70** (1992) 305;
S. Jadach and B.F.L. Ward, Phys. Rev. **D40** (1989) 3582.

[41] S.Jadach *et al.*, *Higher-Order radiative corrections to Bhabha Scattering at low angles: YFS Monte Carlo approach*, CERN-TH /94-38 (Feb.1995).

[42] B.Bloch et al., *Final Luminosity and Systematic errors for 1993 Electroweak Selection*, ALEPH 95-025 (Feb. 1995).

[43] D. Decamp *et al.*, ALEPH Collab., Phys. Lett. **B234** (1990) 209.

[44] D. Decamp *et al.*, ALEPH Collab., Phys. Lett. **B231**,(1989) 519.

[45] D. Buskulic *et al.*, ALEPH Collab., *An Experimental study of* $\gamma\gamma \rightarrow$ *hadrons at LEP*, CERN-PPE/93-94 (June 1993).

[46] A. Blondel, Z. Feng, J. Grahl and J.Harton, *TPC Hadronic Event Selection Point to Point Error and Effect on Z width*, ALEPH 94-106, PHYSIC 94-091 (July 1994);

A. Blondel, Z. Feng, J. Grahl and J.Harton, *Addendum to TPC Hadronic Selection Point to Point Error Study*, ALEPH 94-185, PHYSIC 94-157 (Dec. 1994).

[47] B.Bloch and E. Lancon, ALEPH 93-031, PHYSIC 93-022 (1993).

[48] A. Blondel and E. Blucher, *Hadronic Event Selection with Charged Tracks*, ALEPH 90-171, PHYSIC 90-99 (Nov. 1990).

[49] A. Lucotte, ALEPH 94-170, PHYSIC 94-145 (Nov. 1994).

[50] A. lucotte and F. Teubert, ALEPH 95-035, PHYSIC 95-033 (1995).

[51] J. Harton and M. Sadd, *Z Lineshape Fit with ZFITTER Package*, ALEPH 92-133, PHYSIC 92-122 (1992).

[52] R. Assmann *et al.*, *The Energy Calibration of LEP in the 1993 Scan*, CERN SL/95-02, CERN PPE/95-10 (1995).

[53] D.Bardin *et al.*, *ZFITTER: an Analytical Program for Fermion Pair Production in e^+e^- Annihilation*, CERN-TH 6443/92 (1992).

[54] D. Buskulic *et al.*, ALEPH Collab., *Improved Tau Polarization Measurement*, CERN-PPE / 95-023 (1995).

[55] D.Buskulic *et al.*, ALEPH Collab., Phys. Lett. **B313** (1993) 535;
D.Buskulic *et al.*, ALEPH Collab., Z. Phys. **C62** (1994) 179;
D.Buskulic *et al.*, ALEPH Collab., Phys. Lett. **B335** (1994) 99.

[56] A. Blondel *et al.*, ALEPH 93-44, PHYSIC 93-35 (1993).

[57] V.N. Baier and V.A. Khoze, Sov. J Phys. **9** (1969) 238.

[58] R.Assmann *et al.*, *Polarization Studies at LEP in 1993*, CERN SL/94-08 (March 1994).

[59] M.Froissart and R. Stora, Nucl. Instr. Meth. **7** (1960) 297.

[60] L.Arnaudon *et al.*, *Effect of Tidal Forces on the Beam Energy in LEP*, Proc. of the 1992 Particle accelerator Conference, May 1993, Washington.

[61] L.Arnaudon *et al.*, *Effects of Terrestrial Tides on the LEP Beam Energy*, CERN SL/94-07 (BI) (March 1994).

[62] J.Wenninger, *Study of the LEP Beam Energy with Beam Orbit and Tunes*, CERN SL/94-14 (BI) (April 1994).

[63] G.Fischer and A. Hofmann, *Effects of Tidal Forces on the LEP Energy*, Proc. of the second workshop on LEP machine, J. Poole Editor, CERN -SL / 92-29 (DI).